Interactive comment on "Confinement of air in the Asian monsoon anticyclone and pathways of convective air to the stratosphere during summer season" *by* B. Legras & S. Bucci
Answer to reviewer #1

B. Legras and S. Bucci

Correspondence: bernard.legras@lmd.ens.fr

We thank the reviewer #1 for his/her thorough discussion that led to significant improvements of our manuscript and a reinforcement of our conclusions.

As Fig. 6 has been removed from the paper, a shift in the numbering of the subsequent figures occurs in the new version. We therefore refer to these figures with the new number followed by the old in parenthesis.

Answer to general comments

- *"...The ERA5 diabatic and kinematic results differ not as much from each other than the respective results for ERA-Interim...". An important question is, if this is because the frequency of the data rather than data quality (less noise) became better for ERA5 if compared with ERA-Interim? Thus, if for ERA5 the data frequency would be reduced from 1 hour to 6 hour, would we also get similar large differences between the diabatic and kinematic calculations?*

  First, the ERA-Interim winds are used at 3-hourly resolution because we interleave 3h and 9h forecasts between the analysis, at 0h and 6h, for each 12h assimilation cycle. The heating rates which are a product of the forecast are also used at 3-hourly resolution. The effect of using hourly, 3-hourly and 6-hourly data in the ECMWF operational model for transport studies with TRACZILLA was studied by Pisso et al. (2010) who concluded that the improvement was important from 6-hourly to 3-hourly but was modest from 3-hourly to hourly. On the contrary, Angevine et al. (2014) found than hourly wind were improving the results of FLEXPART but this was for a mesoscale application.

  It would take many efforts to redo our calculations at degraded resolution but one can compare the variances of the heating rates and the velocities shown in Fig. A1-1 in the core of the AMA. The ERA5 hourly variance is much larger than the 3-hourly ERA-Interim variance in the whole TTL for the vertical velocity and up to than 380 K for the heating rate. The variance of ERA5 3-hourly data calculated as averages of the hourly data is, by construction, smaller than that of the hourly data. However, it is much larger than the minimum value that would obtain if the hourly data were decorrelated from one time to the next. This means that a significant correlation of hourly heating rates and vertical velocities persists over three hours and that we do not expect a very significant change by degrading the resolution to 3h. The differences in transport properties with the ERA-Interim are too large to be explained this way.

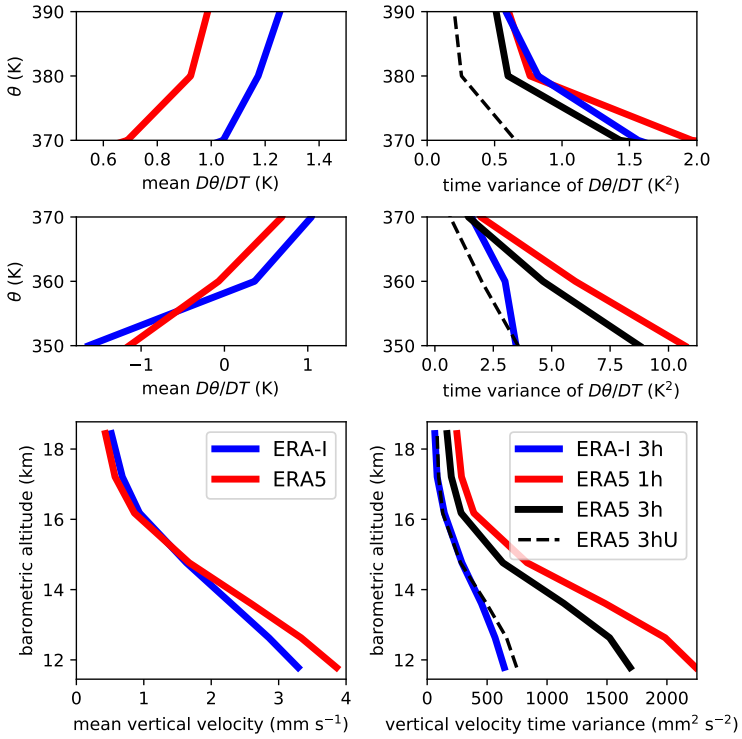

Figure A1-1. Mean profiles (left column) and variances (right column) for the all sky heating rate (2 upper rows) and the vertical velocity (lower row). Blue curves are for the ERA-interim data at 3-hourly resolution, red curves are for the ERA5 data at hourly resolution and black curves are for the averaged 3-hourly ERA5 data. The dashed black curve shows the 3-hourly ERA5 variance under the hypothesis of uncorrelated hourly data which is one-third of the hourly variance. The calculations are performed in the domain (20°E-140°E and 10°N-40°N) over July and August 2017.

– *You do not talk too much about the tropopause, especially as a vertical transport barrier during slow ascent of the spiraling trajectories. Because I do not see any effect of such a barrier in your results, I would recommend to mention this point in your discussion/conclusion or maybe even in the the abstract, i.e. something like: "tropopause is not a transport barrier for the vertically ascending trajectories..."*

We thank the reviewer for raising this point. It is true that the tropopause does not seem to play any particular role in slowing the transport or changing its character. The mean ascent rate of 1.1 Kday^{-1} extends smoothly through it. The important barrier level is the crossover level that one can see, within the diabatic framework, as the Lagrangian mean extension of the zero level of radiative heating rate.

– *This trajectory-based study with "true" convective clouds is very impressive and technically extremely well done. However, this is only an extremely model-based view of transport without any comparison with observations. Because of*

this, the picture of spiraling trajectories is a biased picture of reality (in the same way like "chimney", "conduit" or "blower"). Maybe the authors would like to re-consider this point.

Our approach has been extensively tested against observations up to 400 K in a companion paper (Bucci et al., 2019) where we used the same tools in a comparison of Lagrangian reconstructions with data from the StratoClim campaign. We found that the ERA5 diabatic trajectories provided the best interpretation of the data. Our methods have also identified the sources of ammonium measured at high altitude by following back trajectories spiralling in the AMA to the agriculture sources (Höpfner et al., 2019) and further checks will appear in other works to be published. The robustness of the modelling approach is therefore supported by observations.

– *Horizontal confinement versus vertical transport. You derive some numbers showing that the horizontal confinement of the anticyclone is relatively weak (compared with the circulation rate). I am not convinced that the e-floding times derived from figure 7 really quantity the erosion rate, i.e., bi-directional crossing of air parcels across the vortex edge, a process which is typically believed to define the horizontal confinement (see also the minor comments).*

The erosion time scale 13.3 day is actually quite comparable to the circulation time which is about two weeks. Figure 6(7) is based on the loss rate of the FullAMA box. Therefore, parcels accumulating at the periphery of the anticyclone would not be lost. Figure 8(9) shows that from 370 K to 420 K, the impact pattern remains quasi-constant but for the exponential decay shown in Fig. 6(7). There is no accumulation on the edge or elsewhere that builds up. A fit to the exponential decay of the total impact with altitude between 370 K and 400 K gives a slope of 0.065 K^{-1} which is to be compared to the inverse of the product between the ascent rate 1.1 $\mathrm{K day}^{-1}$, that is 0.068 K^{-1}. Therefore, all the pieces fit together and the exponential rate found in Fig. 6(7) is a good representation of the erosion rate.

– *The 1d model is a great mathematical tool to put many things together and to create a simply 1d picture. But it is too much for this paper. Maybe to divide the whole material into two parts would help.*

We consider that the 1-D model is an important part of the paper as it fulfils the demonstration that the average transport properties of the Asian Monsoon Anticyclone can be quantitatively reduced to a small set of simple parameters. Without that part, we think that the paper will be considerably weakened. We notice that the reviewer considers below that one of the figure produced from the 1-D model is so important that it should be moved from the supplement to the main text.

Answer to minor comments

Some of these comments might have deserved to be in the major section but we follow the ordering of the reviewer.

– *P1, L24 "due to a dominant radiative cooling" - not clear. Ascending motion means increase of the potential temperature of the considered air parcel. This means absorption of energy or warming. Maybe you should clarify this point.*

The main detrainment of the convective clouds occurs at a level below the level of zero radiative heating (LZRH) where the air is almost everywhere descending. This is accompanied by radiative cooling. It has been often questioned

how this air could find its way above the LZRH (Corti et al., 2006). Our answer is that it does not. The LZRH or its Lagrangian version we call the crossover is a barrier and only clouds detraining above can feed the mass flux that enters the stratosphere.

– *P2 L20-25 In your abstract you write: "We find no trace of a vertical conduit above convection over the Tibetan plateau": Maybe you should discuss in this paragraph also the concept of conduit and the related literature (mainly Bergman at al. papers). Furthermore, you discuss the concepts of "chimney" and "spiraling ascent" as two "extreme views". Please do not forget that the concept of "spiraling ascent" (which you seem to like more) is strongly related to long-term (40 days or more) and non- mixing trajectories. This is also a strong idealization, without any experimental confirmation in the observed tracers.*

This is an important point that has led us to add some text in Sec. 3.3 and to rephrase a few sentences in the conclusions. We essentially recover the results of Bergman et al. (2013) in the compact distribution of sources shown in Fig. 8(9) and even more explicitly in Fig. 10(11) that shows the sources of backward trajectories similar to those they calculated. In our set-up, the high convective sources are assumed to loft parcels directly from the boundary layer located about 15 km beneath. This is what accounts of the conduit found in Bergman et al. (2013). The main interest of our work is that we separate the fast vertical transport that occurs in the cloud and the much slower transport of detrained parcels that occurs outside the convective towers. It is this second part which is the focus of this work. It is much more difficult to make such separation when doing calculations based on reanalysis winds down to the surface since the vertical velocities in the convective layers are averages of upward and downward motion at the mesh size. These velocities do not represent the speed of the transport of the surface to the TTL which takes a few weeks instead of a few tens of minutes. This smooth transport does not see the clouds and cannot say where the conduit ends. Our answer is that it ends at the detrainment level of the clouds. The clouds that provide air entering the stratosphere are those that reach above the crossover which is quite uniform over whole Asia. This crossover is located slightly above the continental LZRH and this is expected from the 1D model if diffusion due to heating variance does not play a significant role. The Tibetan plateau is the only region where the crossover is below the LZRH. This means that the parcels need to leave the Tibetan plateau to rise to higher altitude. This is what they do following the spiralling paths we have identified. This spiralling motion is not an idealization or a numerical fantasy, there are plenty of confirmations by observations in the analysis of the StratoClim data (see Höpfner et al., 2019; Bucci et al., 2019). it is the very essence of motion within the AMA.

On the other side, our results are also compatible with the findings of Ploeger et al. (2017) who launched forward trajectories near 360 K. The impact pattern being almost constant with height preserves a maximum at the core of AMA at high altitude as noticed by Ploeger et al. (2017). However, this does not imply per se that transport is more vertical than horizontal across a given surface like the tropopause. This property depends a lot on the slope of this surface with respect to the isentropes. Our analysis which is conducted from the potential temperature perspective does not exhibit any discontinuity in the range of levels spanned by the tropopause. Our simple 1D view of constant ascent and constant is, on the seasonal average, essentially valid from the crossover at 364 K to 420 K.

See also our discussion of the backward versus forward trajectories below.

– *P2 L34 "We also focus on reconciling previous studies...": This is for me too strong. The presented study including the 1D-model, does not contain any comparison with the experimental data. With the 1D-model you can get a different perspective on the presented, 3d-trajectory-based results. However, as mentioned above, I would recommend to have a separate paper describing the 1D model.*

Again, look at Bucci et al. (2019) regarding direct comparisons with tracer data. Our claim is that the main features of the mean 3D transport can be represented quantitatively in terms of a few parameters and that this is quantitatively equivalent to a simple 1D model. Physics is full of other examples where a mean field theory describes the mean behaviour of an apparently very complex system.

Our discussion is able to include the findings from previous studies and to provide a new interpretation for some of them that eliminates the apparent contradictions. For instance, we show that the existence of a columnar tracer pattern within the AMA, cannot be taken as a proof that the AMA behaves as a closed "chimney" with no leak as it has been often assumed on the basis of a qualitative interpretation. We show that the chimney hypothesis is contradicted by the detailed analysis of the transport properties and that instead the columnar tracer pattern is compatible with the broad ascent with uniform loss that is the product of the transport. Observations are not limited to tracers but include temperatures and winds which are assimilated to produce the velocity fields. There is no doubt that state of the art NWP systems produce analysed horizontal winds which are a good approximation of the true circulation. Our work is investigating the consequences of these observations within the well validated framework of geophysical fluid dynamics. It is therefore incorrect to say that we do not take account of experimental data. We actually take account of both tracer and dynamical observations and we arrive at a new interpretation that is not contradicted by any of them. This is the way in which we reconcile the previous studies which did not adopt this global perspective.

– *P3 L21 Maybe you can finish the sentence in L21: "...at a 0.25 0 horizontal resolution.", skip the lines 22 and 23 and follow with "The data are availably..." FullAMA will be explained in section 2.3.*

Good suggestion. We have done that.

– *P3 L29 ...cloud radiative heating (CRH) : Is it calculated as "all sky heating" - "clear sky heating"?. It would be nice to mention it either in the text or in the caption of Figure 1. The green contour for ERA5 around the the equator between 17.5 and 20 km looks strange for me.*

The cloud radiative heating is calculated in that way, now mentioned in the text. The green contour at the equator above the tropopause comes from the data. It corresponds to a descent in the stratosphere by 20 km above the equator that is modulated by the QBO. This feature exhibits some slight variability among the reanalyses.

– *P4 L10 Are both terms: "latent heat" and "vertical heat diffusion" really available in both reanalysis products ERA-Interim and ERA-5?*

No, there is a total temperature tendency and there are all sky and clear sky long wave and short wave heating rates. The residual, latent heating + diffusion, can be obtained by subtracting the all sky heating rate from the total. There is also a separate heat coefficient diffusion which might help to reconstruct the vertical heat diffusion. We have changed the sentence to avoid suggesting the two quantities are separately available.

- *P4 L12-13 I think, Ploeger et al., 2017 does not initialize the tracers in the boundary layer but above theta=360 K. Please reformulate.*

  Corrected.

- *P4 L14 ...converges rapidly to the (clear sky) radiative heating rate as a...*

  It is not only clear sky. Radiative heating by clouds cannot be neglected even high above their top. For instance high opaque clouds reduce significantly the upward long wave flux in the whole column above their top. It was proposed by Corti et al. (2006) that the warming produced by overlaying cirrus helps parcels to cross the LZRH. What we neglect here is the cooling effect due to the evaporation of falling ice in clear air.

- *P4 L19 ...for several levels during summer 2017...*

  Corrected

- *P5 L2 S2 Montgomery potential. I did not find the derivation of (1) in Nakamura at al., 1995. Maybe this is the wrong citation or you should reference more exactly the used equation.*

  The derivation is not in Nakamura (1995) but it can be easily derived using the framework of this work. We provide now a more detailed derivation as this relation might be of some practical usage.

- *P5 L 5 Sattellitte - please correct*

  Correction done

- *P5 L 11 in the FullAMA domain...?*

  Correction done.

- *P5 L21 "For each of these cloud pixels"...maybe better: "For each of the selected cloud pixels"*

  Correction done

- *P5 L27 "...version is labeled EAZ. Additional two integrations..." - sounds better for me*

  Correction done

- *P5 L34 "every 15' and 20": I would mention that this is the temporal resolution (see also L8)*

  Correction done

– *P6 L13-14 It would be nice to know how the units of the convective impact factor shown e.g. in Fig. 2 (day 2 /K) can be derived from your impact density*

There was a typo error in the normalizing formula given in Sec. 2.5. $\Delta\theta$ should not appear with an exponent 2 in the denominator. So $\mathrm{day}^2\mathrm{K}^{-1}$ is the correct unit for impact density. Therefore the cumulated age is using $\mathrm{day}^2\mathrm{km}^2\mathrm{K}^{-1}$ units and the age histogram (in Fig.5) is using $\mathrm{day\,km}^2\mathrm{K}^{-1}$ units. Thanks for spotting that. The units used in the figures were correct. We also use the equalized impact density which is without unit.

– *P6 L18-20 ...do not understand. sorry*

These lines have been rewritten.

– *P6 L23 "The impact can also be stratified according to": I am not sure that this is the best English formulation. Maybe "spectral-resolved with respect to age", how- ever,"stratified" is certainly shorter*

This sentence has been removed as the age is only needed in Sec. 3.4. We now prefer "sorted" to "stratified".

– *P7, L2 "...and decays from 0.88 at 350K to 0.52 at 420K" 0.5 at 420K is really small. It means that only 50the FullAMA region are correctly counted. However, we are more interested in the air masses entering the stratosphere through the anticyclone and not through the FullAMA region. Maybe it would be better to calculate the accumulated impact for the AMACore rather than for the FullAMA region.*

At 420 K, the dilution is of a factor 26 with respect to the level 370 K and the air composition is dominated by the stratospheric background (as confirmed by unpublished observations of the StratoClim campaign). What we count are the parcels in the FullAMA domain which never leave the domain. The many parcels that leave the domain below 420 K still climb to higher levels in the outside world and can later re-enter the FullAMA domain after completing a large loop or, most often, a full latitude circle. This might be a debatable issue but we tend to consider these parcels as not different from the background and no longer as fresh convective particles as they have been transported over long distances in filamentary structures that have been strained and stretched a lot resulting in mixing with surrounding air. It is nevertheless possible that a significant convective influence is preserved at 420 K within the AMA like at 400 K (as shown from backward calculations).

The FullAMA domain has been chosen in such a way that almost all parcels leaving the anticyclone are also leaving the domain soon after. This was done in order to avoid resorting to an a priori definition of the AMA boundary which presents considerable difficulties on a day to day basis. The AMACore domain remains most of the time inside the AMA but there is no reason to assume that the parcels spend most of there time in this domain. Figure 10(11) actually shows they tend to be ejected to the periphery.

– *Figure 3 The used notation in this figure should be the same as in the main text (AMA → FullAMA, ("max global" P and "max ERAI" is the same, maybe "max global (ERAI)", and the same with the ...)*

We agree that it was quite difficult to follow this discussion. Fig. 3 is now better referred in the text.

– *P 8 L 21 ...Figure 4, bottom panel shows the distribution....*

Corrected, this was a relic of a previous different layout.

– *P 8 L 22 You can use your abbreviation AMACore...*

We have removed this acronym as it was used only a couple of times and therefore was no necessary.

– *P 8 L 29 ...propagates inside the FullAMA (?) domain from the sources...*

Corrected

– *P 8 L 34 Supplement: S3 is not used in the main text. Nevertheless it is interesting Maybe you can couple it with your main text.*

It is indirectly used in Sect. 3.2 when we refer to Sect. S2 of the Supplement.

– *P 8 L 34, Supplement S4 "The normalized impact then becomes an age spectrum...". In this definition of the age spectrum, mixing is not included. Although I know that this concept follows the idea of "irreducible air parcels" (e.g. Schoeberl et al., 2000), however, this is not the way how the age spectrum should be defined by integral operator replacing the full 3d advection-diffusion equation.*

Some sort of mixing is actually present here under the form of time averaging statistics which is equivalent to real mixing under a statistically stationary assumption and our approach could be given an integral representation. Irreducible air parcels are most often used to solve problems which have also an integral representation (see, e.g., Legras et al., 2005). Our definition of the age spectrum does not differ from the common usage.

– *P 9 L 8-9 "As the vertical velocities are ascending everywhere" - All sky radiation in Fig. 4 shows negative values below 360 K both for ERA-I and ERA-5...? You mean the total diabatic heating rates and w in the kinematic case which are shown in S5? "must is located" - must be located.*

Vertical velocities mean Dz/dt, nothing to do with heating. This paragraph has been rewritten and is hopefully more readable. When total diabatic heating, including latent heating, is included, an ascending motion results everywhere in the monsoon region. We have done calculations with the total heating version of the ERA5. Above the crossover the results are almost the same as those obtained with the radiative heating only, so all the conclusions of our work are unchanged. Below the crossover the results are closer to that of the kinematic calculations. We considered that this was sort of expected (and reassuring) and decided it was not necessary to include these results.

– *It seems that there are few good arguments supporting the kinematic approach to quantify the impact density at 340 and 350 K levels (descending branches of the Hadley and of the Hadley-Walker circulations). Maybe it is better to start your arguments with ERA-Interim (Figs. S9 and S10, where these branches are more visible) and continue with ERA-5 (Figs. S7 and S8). I also think that the partition of text (and arguments) between the main text and the supplement can be improved.*

This would lead to a long discussion but we do not see why the kinematic approach is inadequate to describe the descent over the subsident regions of the Hadley-Walker circulation which are essentially free of clouds. The kinematic calculation misses the descent in the monsoon region but this is not the main part of the returning flow and we cannot say that our radiative calculations are very accurate in the range of altitudes below the anvils. In this domain, the local potential temperature profiles undergo frequent inversions due to convective mixing combined with horizontal transport and we neglect cooling by evaporation of stratiform precipitations. Generally speaking, potential temperature is hardly usable as a vertical coordinate in the convective layers of the atmosphere.

- *P 9 L 17 Once again, this is for me not the clean definition of the age spectrum (see above)*

  See answer above.

- *P 9 L 19 "The fastest propagation by EAD....while the slowest propagation by EID" - I think EAD and EID should be exchanged*

  There was an inversion but Fig. 6 has been removed as it brought nothing necessary and could be miss interpreted.

- *Figure 8 The colors are not explained. Also it is not clear if the total impact is calculated for FullAMA or AMACore ?*

  This refers probably to Fig. 6(7) where the indication of the colours was indeed missing in the caption. The total impact is calculated in the FullAMA domain.

- *P 9 L 34 What did you assume for A? According to your equation, A = 1/(0.69α), it will lead to A = 0.109 K/day. I do not see in Figure 4b that this is the mean value of the diabatic ascent. On the other hand, you use in your 1d model values of A = 1 K/day. Please clarify*

  There was a decimal missing in both numbers (0.069 and 0.065). Thank you for spotting that. A is not derived from this formula but from the mean ascent rate in Fig. 5. The inverse of the product $A\alpha$ is compared to the impact slope in the upper panel of Fig. 4.

- *P 9 L 34 I am also not really convinced that α = 13.3 day derived from Figure 7 can be understood as the erosion rate. Clear, the number of convective air parcels is becoming smaller with the altitude because, as you show, the total convective impact decreases with the altitude. But it is not clear, if these air parcels stay e.g. at the (inner) edge of the anticyclone (with low diabatic heating rates) or really cross this edge and move, roughly isentropically, into the regions outside of the anticyclone (such crossing of the edge could be interpreted as the erosion of the anticyclone).*

  This question is already asked in the main comment on the erosion rate and answered above. The parcels need to cross the edge as they cannot leave the FullAMA domain otherwise. If parcels are removed from FullAMA domain, they are a fortiori removed from the AMA. There is no other way.

- *P 9 L 34 If your calculation is correct, you get a picture of "upward spiraling air within a chimney" crossing the tropopause and maybe crossing the edge of the anticy- clone (see above). The latter behaviour, above the tropopause, is sometimes de- noted as a blower.*

The erosion rate is quite uniform above 370 K. There is no indication that the parcels stay inside the AMA seen as a wide chimney and that they are blown away only when they reach sufficiently high. The notion of a blower is correct if it is not localized only above the tropopause but uniformly distributed in potential temperature above the crossover. The idea of a chimney is incorrect as it implies that nothing leaks outside its wall (otherwise it cannot be considered as a good chimney).

- *P 10 L6-24 This part of the text is very similar to the discussion on page 9, L8-15. The figures 8 and 9 are almost the same like figures S7 and S8 discussed before. I think, the logic can be improved here. An idea for the sensitivity study would be to check how your results (total impact) will change if you confine your region from FullAMA to AMACore defined by different values of the Montgomery stream function.*

  Actually, we refer to figures S7 and S9 of the supplement but only to provide supplementary information with respect to the discussion of figure 8 regarding the descent branches and the global versus FullAMA description. The core of the discussion is, however, contained in the main text. We do not see in which way Figs. 7(8) and 8(9) are almost the same. Fig. 7(8) shows the descending branch and the crossover and Fig. 8(9) shows the similarity of the ascending branch.

- *Figure 10 The characters of the potential temperature values in the last column are too small I also think that this figure can be moved to the supplement.*

  The right panels of the figure have been improved. We still think that this figure is useful as the design of the backward calculations is quite similar of that of Bergman et al. (2013) and allows to interpret their finding of a vertical "conduit". This figure also shows the in-mixing of background air (loss of backward trajectories to the background) as a function of altitude and is critical to answer one of the questions of the reviewer below.

- *P 11 L4 ...contribution of sources as the altitude rises...*

  Modified

- *General In all your pictures it is difficult to localize the Tibetan Plateau.*

  We have added a contour for the Tibetan plateau on all the panels describing the sources.

- *Figure 11 Left column: This is a very nice way to show how the spiraling stars in the center of the anticyclone (or spiraling within the chimney). Right column: why you do not use the same color bars like in the left column. I would expect the same spatial distribution of the mean age like in the left column. Because of this, figures (h) and (j) look very confusing for me.*

  Although the range of ages should not be that different, the weighting is very different in the target and the source space and there is no correspondence between cells with a given value in the target space and cells with the same value in the source space. Same remark holds for the impact shown in Figs. 7(8) and 8(9). If there was a preferred conduit from the sources to the 380 K level or the tropopause, this would shown up as a minimum age in the AMA core. This is not the case and we must reject the hypothesis of such a preferred conduit.

– *P 11 L32 maybe: ...in reanalysis-based cloud properties and...*

Modification done.

– *P 12 L30-37 Here I lost your way of arguments. Maybe a stronger relation to the lines in the table and more small-steps explanation of the numbers (like 2.57, 0.41 or "inverted contribution") would help*

We have rewritten and hopefully improved the description and the discussion of the crossover which is a central result of our work.

– *P 13 L 13 You should give here the definition of* $S = S_0 exp - \beta$ *...*

Actually, it has to be given a bit below as $S(\theta)$ in (1) can also be the observed distribution from the SAF-NWC products.

– *P 13 L 23 "Consequently, the distribution of convective sources..." I thought that this distribution is prescribed by S. Maybe you mean the distribution of air parcels originating from the convective sources.*

This was confusing and has been corrected. We mean the distribution of convective parcels that reach a given level. The factors depending on this level are contained in the constant N.

– *P 14 L 5 I think, the figure S12 is so important to understand the 1d-model that it cannot be moved to the supplement. By the way, I did not find at which level all the distributions are shown in figure S12.*

We followed the advice of the reviewer and moved this figure to the main text, merging it with Fig. 13(14) so that the number of figures does not increase. The figure are plotted at $\theta = 380$ K.

– *P 14 L 5 Parameter* α *describing the erosion rate. It is not clear if this parameter in the 1d-model is the same like that introduced in 3.2. The numbers seem to be very different. In relation to the 1d-model you do not introduce it in the main text and even in the supplement you do not say what is the basic value of* α *(S9 L8-10).*

The basis parameters at the second stage of the 1D model include $\alpha = 10$ day as only the order of magnitude is needed to show the sensitivity to variations of parameters. In the third stage which is directly compared to the 3D trajectories, we use $\alpha = 13.3$ day that is the value derived in Sec.3.2. This should be now clear in the text.

– *P 14 L 19 "...provide a consistent description.." - see my first main comment.*

Please refer to our answer above.

– *P 14 L 31 "...leaky circulation..." - I do not see a good proof of this statement (see my comments above)*

Please refer to our answer above.

– *P 15 L 1-2 "...As the level rises, the confined Asian monsoon is more and more diluted..." - same type of problem. See also abstract: "The contrast is reduced by dilution...". Which type of dilution: in-mixing of old stratospheric air into the anticyclone? But you do not have any proof of that.*

The in-mixing from the background is demonstrated in the backward calculations (as an increasing amount of backward trajectories come from the background with increasing height). This is consistent with all the other results of our study.

It is useful to compare the backward hit percentage and the forward impact. If we consider the two levels 380 K and 400 K in Fig. 9(10), the areas of backward hit percentage larger than 70% for the first and 30% for the second are fairly similar, 15.210^6 km^2 and 16.110^6 km^2 respectively, and cover a large portion of the AMA domain, whatever definition is used. This shows obviously that the convective influence propagates high in the lower stratosphere and that the in-mixing of background air is very limited. However, the ratios of the forward cumulated impact contained in these areas to that in the same areas at 355 K where it is maximum can also be calculated and are only 12% and 4,5 respectively. There is no paradox, it only means that air escapes easily from the AMA as it ascends but penetrates much less easily inside. The distribution of backward hit percentage is also compatible with the observation of an apparent plume of tropospheric tracer in the AMA which has been reported in several previous studies based on large scale data and large-scale models (Park et al., 2009; Randel et al., 2010; Pan et al., 2016, e.g.). A columnar AMA rich in parcels influenced by convection and surrounded by background air is producing this very pattern. Therefore we prove that observing such a tracer columnar pattern is not a proof of a chimney with impermeable walls as it is often assumed. It is generally known (see, e.g. Joseph and Legras, 2002) that forward trajectories link the stable structures at the initial point to the unstable structures at the final point in the future, while the backward trajectories link the stable structures at the initial point to the unstable structures at the final point in the past. Here the backward trajectories link the confined domain of the AMA to the LZRH surface, around which they tend to oscillate at long time while this same surface repels forward trajectories. This paragraph has been added to Sec. 3.3

– *P 15 L 18 "...rather than concentrated in a narrow pipe." - It means for me, it is certainly not a conduit but much more a chimney, with some upward spiraling air inside.*

A chimney with walls at the edge of the AMA is excluded by our analysis as discussed in the previous comments and we demonstrate that the observation of a columnar pattern of tropospheric tracer within the AMA cannot be taken as a proof of a chimney.

References

Angevine, W. M., Brioude, J., McKeen, S., and Holloway, J. S.: Uncertainty in Lagrangian Pollutant Transport Simulations Due to Meteorological Uncertainty from a Mesoscale WRF Ensemble, Geoscientific Model Development, 7, 2817–2829, https://doi.org/10.5194/gmd-7-2817-2014, 2014.

Bergman, J. W., Fierli, F., Jensen, E. J., Honomichl, S., and Pan, L. L.: Boundary Layer Sources for the Asian Anticyclone: Regional Contributions to a Vertical Conduit, Journal of Geophysical Research: Atmospheres, 118, 2560–2575, https://doi.org/10.1002/jgrd.50142, 2013.

Bucci, S., Legras, B., Sellitto, P., D'Amato, F., Viciani, S., Montori, A., Chiarugi, A., Ravegnani, F., Ulanovsky, A., Cairo, F., and Stroh, F.: Deep Convective Influence on the UTLS Composition in the Asian Monsoon Anticyclone Region: 2017 StratoClim Campaign Results, Atmospheric Chemistry and Physics Discussions, https://doi.org/10.5194/acp-2019-1053, 2019.

Corti, T., Luo, B. P., Fu, Q., Vömel, H., and Peter, T.: The Impact of Cirrus Clouds on Tropical Troposphere-to-Stratosphere Transport, Atmospheric Chemistry and Physics, 6, 2539–2547, https://doi.org/10.5194/acp-6-2539-2006, 2006.

Höpfner, M., Ungermann, J., Borrmann, S., Wagner, R., Spang, R., Riese, M., Stiller, G., Appel, O., Batenburg, A. M., Bucci, S., Cairo, F., Dragoneas, A., Friedl-Vallon, F., Hünig, A., Johansson, S., Krasauskas, L., Legras, B., Leisner, T., Mahnke, C., Möhler, O., Molleker, S., Müller, R., Neubert, T., Orphal, J., Preusse, P., Rex, M., Saathoff, H., Stroh, F., Weigel, R., and Wohltmann, I.: Ammonium Nitrate Particles Formed in Upper Troposphere from Ground Ammonia Sources during Asian Monsoons, Nature Geoscience, 12, 608–612, https://doi.org/10.1038/s41561-019-0385-8, 2019.

Joseph, B. and Legras, B.: Relation between Kinematic Boundaries, Stirring, and Barriers for the Antarctic Polar Vortex, Journal of the Atmospheric Sciences, 59, 1198–1212, https://doi.org/10.1175/1520-0469(2002)059<1198:RBKBSA>2.0.CO;2, 2002.

Legras, B., Pisso, I., Berthet, G., and Lefèvre, F.: Variability of the Lagrangian Turbulent Diffusion in the Lower Stratosphere, Atmospheric Chemistry and Physics, 5, 1605–1622, https://doi.org/10.5194/acp-5-1605-2005, 2005.

Pan, L. L., Honomichl, S. B., Kinnison, D. E., Abalos, M., Randel, W. J., Bergman, J. W., and Bian, J.: Transport of Chemical Tracers from the Boundary Layer to Stratosphere Associated with the Dynamics of the Asian Summer Monsoon, Journal of Geophysical Research: Atmospheres, 121, 14,159–14,174, https://doi.org/10.1002/2016JD025616, 2016.

Park, M., Randel, W. J., Emmons, L. K., and Livesey, N. J.: Transport Pathways of Carbon Monoxide in the Asian Summer Monsoon Diagnosed from Model of Ozone and Related Tracers (MOZART), Journal of Geophysical Research, 114, D08 303–D08 303, https://doi.org/10.1029/2008JD010621, 2009.

Pisso, I., Marécal, V., Legras, B., and Berthet, G.: Sensitivity of Ensemble Lagrangian Reconstructions to Assimilated Wind Time Step Resolution, Atmospheric Chemistry and Physics, 10, 3155–3162, https://doi.org/10.5194/acp-10-3155-2010, 2010.

Ploeger, F., Konopka, P., Walker, K., and Riese, M.: Quantifying Pollution Transport from the Asian Monsoon Anticyclone into the Lower Stratosphere, Atmospheric Chemistry and Physics, 17, 7055–7066, https://doi.org/10.5194/acp-17-7055-2017, 2017.

Randel, W. J., Park, M., Emmons, L., Kinnison, D., Bernath, P., a Walker, K., Boone, C., and Pumphrey, H.: Asian Monsoon Transport of Pollution to the Stratosphere., Science, 328, 611–613, https://doi.org/10.1126/science.1182274, 2010.

Interactive comment on "Confinement of air in the Asian monsoon anticyclone and pathways of convective air to the stratosphere during summer season" *by* B. Legras & S. Bucci
Answer to reviewer #2

B. Legras and S. Bucci

Correspondence: bernard.legras@lmd.ens.fr

We thank reviewer #2 for his/her comments.

Answer to general comment

0.1 On the overall sloppiness in the layout and presentation

As the opinion of the second reviewer is quite contrasted with that of the first reviewer who wrote that the paper is well-written, we beg the second reviewer to forgive our poor English style but we disagree that our paper is not constructed. We worked on the text to improve the readability of the manuscript and, in particular, to rework the single sentence paragraphs.

0.2 On the robustness of the results

We are aware of the possible impact of the duration of numerical calculations on the statistics built from time integrals. The 2-month integration time has been precisely chosen to avoid such effects and all the displayed results are robust in this respect. The impact is shown in Fig. 5 and in Fig. S5, as a function of age, after normalization on each level. As these figures use a logarithmic scale, it is clear that very little contribution to low order moment statistics can arise from ages larger than two months except at the top levels above 380 K for EIZ and above 400 K for the other cases. In order to show this better, Fig. A2-1 compares, for the four cases of Fig. 5, the mean ages obtained by averaging over the two months period and after applying the exponential tail correction of Scheele et al. (2005),

$$\mathcal{A}_c = \frac{\mathcal{A} + \frac{F_f}{b}\left(\tau_f + \frac{1}{b}\right)}{1 + \frac{F_b}{b}}\,, \tag{1}$$

where $\mathcal{A}$ is the uncorrected mean age, $\mathcal{A} = \sum_{i=0}^{P-1} F_i \tau_i \delta\tau$, calculated from the normalized impact histogram $\{F_i\}$ over P bins of width $\delta\tau$ in the age between 0 and τ_f, and $-b$ is the slope of the exponential tail. Here the slope is calculated for all the levels between $\tau = 50$ days and $\tau = 62$ days and its value is averaged between 330 K and 390 K.

Figure A2-1 shows that, for all cases but EIZ, the correction is fully negligeable up to 400 K and is still small at 420 K. The results described from Sec. 3.3 onward are mostly limited to below 400 K and to the diabatic cases. EAZ results are used in

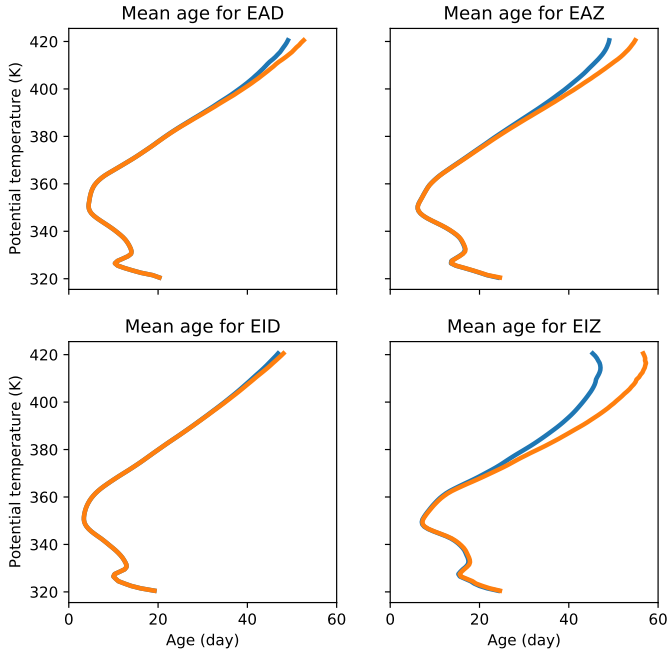

Figure A2-1. Uncorrected mean age (blue) and corrected mean age using (1) (orange) as a function of potential temperature for the four cases EAD (ERA5 diabatic), EAZ (ERA5 kinematic), EID (ERA-Interim diabatic) and EIZ (ERA-Interim kinematic).

the supplement up to 400 K and EIZ is used in Fig. S10 but to show differences between kinematic and diabatic transport in the Hadley-Walker domain, that is at low altitudes. It is also clear that estimates of the ascent rate following the modal peak are not affected, even at 420 K. Figure A2-1 has been added to the Supplement.

Figure 6 was meant to show the difficulties that arise when using average metrics. As it is unecessary to the paper and is a source of confusion, it has been removed.

0.3 On the inconsistency of vertical motion with observed clouds

The reviewer points here to an important limitation of our approach that combines analysed velocities and heating rates with observed clouds. In the present state of the art, the reanalysis do not assimilate any cloud observations (besides winds derived from cloud motion) and therefore the model clouds are generated by the model parametrization. Although extensive comparisons demonstrate the ability of NWP models to predict the cloud cover and precipitation, observed clouds and model clouds most generally do not coincide at local scale in timing, position and extent. Therefore the cloud effects on vertical and horizontal transport also differ in the model and in the real atmosphere. Our approach assumes that the relaxation time of such effects which is up to several days in the TTL, is large enough, with respect to cloud time scale, to ensure a statistical smoothing of the cloud effects that brings the transport properties of the model close to the observations. This assumption has been used already in a number of previous works (e.g. Pfister et al., 2001; Luo and Rossow, 2004; James et al., 2008; Bergman et al.,

2012; Ueyama et al., 2014; Tissier and Legras, 2016). Our present approach has been recently tested in the context of the Asian monsoon by a detailed comparison of Lagrangian trajectories with airborne tracer data (Bucci et al., 2019).

0.4 On the usage of acronyms

We agree that the usage of non standard acronyms should be limited but they are somewhat necessary when the same objects are mentioned in multiple instances within a text. We use here four specific acronyms to designate the reanalyses which are each used between 20 and 30 times in the main text and the supplement and the word FullAMA that denote our main region encompassing the Asian Monsoon Anticyclone is used about 60 times. We do not think that replacing them by expanded expression would improve the manuscript. We have however expanded the EAD, EAZ, EID and EIZ acronyms in most of the captions. The AMACore acronym which was not necessary has been removed.

0.5 On the 1-D model

We consider that the 1-D model is an important part of the paper as it fulfils the demonstration that the average transport properties of the Asian Monsoon Anticyclone can be quantitatively reduced to a small set of simple parameters. Without that part, we think that the paper will be considerably weakened.

0.6 Minor comments

We have made all the required changes.

References

Bergman, J. W., Jensen, E. J., Pfister, L., and Yang, Q.: Seasonal Differences of Vertical-Transport Efficiency in the Tropical Tropopause Layer: On the Interplay between Tropical Deep Convection, Large-Scale Vertical Ascent, and Horizontal Circulations, Journal of Geophysical Research, 117, D05 302, https://doi.org/10.1029/2011JD016992, 2012.

Bucci, S., Legras, B., Sellitto, P., D'Amato, F., Viciani, S., Montori, A., Chiarugi, A., Ravegnani, F., Ulanovsky, A., Cairo, F., and Stroh, F.: Deep Convective Influence on the UTLS Composition in the Asian Monsoon Anticyclone Region: 2017 StratoClim Campaign Results, Atmospheric Chemistry and Physics Discussions, https://doi.org/10.5194/acp-2019-1053, 2019.

James, R., Bonazzola, M., Legras, B., Surbled, K., and Fueglistaler, S.: Water Vapor Transport and Dehydration above Convective Outflow during Asian Monsoon, Geophysical Research Letters, 35, L20 810, https://doi.org/10.1029/2008GL035441, 2008.

Luo, Z. and Rossow, W. B.: Characterizing Tropical Cirrus Life Cycle, Evolution, and Interaction with Upper-Tropospheric Water Vapor Using Lagrangian Trajectory Analysis of Satellite Observations, Journal of climate, 17, 4541–4563, 2004.

Pfister, L., Selkirk, H. B., Jensen, E. J., Schoeberl, M. R., Toon, O. B., Browell, E. V., Grant, W. B., Gary, B., Mahoney, M. J., Bui, T. V., and Hintsa, E.: Aircraft Observations of Thin Cirrus Clouds near the Tropical Tropopause, Journal of Geophysical Research: Atmospheres, 106, 9765–9786, https://doi.org/10.1029/2000JD900648, 2001.

Scheele, M. P., Siegmund, P. C., and Velthoven, P. F. J.: Stratospheric Age of Air Computed with Trajectories Based on Various 3D-Var and 4D-Var Data Sets, Atmospheric Chemistry and Physics, 5, 1–7, https://doi.org/10.5194/acp-5-1-2005, 2005.

Tissier, A.-S. and Legras, B.: Convective Sources of Trajectories Traversing the Tropical Tropopause Layer, Atmospheric Chemistry and Physics, 16, 3383–3398, https://doi.org/10.5194/acp-16-3383-2016, 2016.

Ueyama, R., Jensen, E. J., Pfister, L., Diskin, G. S., Bui, T. P., and Dean-Day, J. M.: Dehydration in the Tropical Tropopause Layer: A Case Study for Model Evaluation Using Aircraft Observations: A Case Study of TTL Dehydration, Journal of Geophysical Research: Atmospheres, 119, 5299–5316, https://doi.org/10.1002/2013JD021381, 2014.

Confinement of air in the Asian monsoon anticyclone and pathways of convective air to the stratosphere during summer season

Bernard Legras and Silvia Bucci

Laboratoire de Météorologie Dynamique, UMR CNRS 8539, IPSL, PSL-ENS/Sorbonne Université/Ecole Polytechnique, Paris, France

Correspondence: Bernard Legras (bernard.legras@lmd.ens.fr)

Abstract. We study the transport pathways from the top of convective clouds to the lower tropical stratosphere during the Asian monsoon, using ~~massive~~ a dense cover of Lagrangian trajectories driven by observed clouds and the two ~~reanalysis~~ reanalyses ERA-Interim and ERA5 with diabatic and kinematic vertical motions. We find that the upward propagation of convective impact is very similar for the kinematic and diabatic ~~calculations~~ trajectories using ERA5 while the two cases strongly differ for ERA-Interim. The ~~separation of descending and ascending motion occurs at a crossover level which is slightly above the all sky zero level of radiative heating rate, except over the Tibetan plateau. The~~ parcels that stay confined within the Asian monsoon anticyclone and reach 380 K are mostly of continental origin while maritime sources are dominating when the whole global 380 K surface is considered. ~~We find that the~~ Over the continent, the separation of descending and ascending motion occurs at a crossover level near 364 K which is slightly above the all sky zero level of radiative heating rate, except over the Tibetan Plateau. The strong impact of the Tibetan ~~plateau~~ Plateau with respect to its share of high clouds is entirely due to its elevated proportion of high clouds above the crossover. ~~We find no trace of a vertical conduit above convection over the Tibetan plateau; parcels are rather entrained into~~ The vertical conduit found in previous studies actually ends where the convective clouds detrain. Subsequent parcel motion is characterized by an ascending spiral ~~motion~~ that spans the whole anticyclone. The mean age of parcels with respect to convection exhibits a minimum at the centre of the Asian monsoon anticyclone, due to the permanent renewal by fresh convective air, and largest values on the periphery as air spirals out. ~~The~~ This contrast is reduced by dilution for increasing ~~potential temperature. We find that the confinement above~~ altitude. Above 360 K, the confinement can be represented ~~, on the average,~~ by a simple 1D process of diabatic advection with loss. The mean loss time is about 13 days and uniform over the range 360 K to 420 K which is to be compared with a total circulation time of two to three weeks around the anticyclone. The vertical dilution is consequently exponential with an e-folding potential temperature scale of 15 K (about 3 km). The mechanism is compatible with the appearance of a columnar tracer pattern within the anticyclone. It is noticeable that the tropopause does not exhibit any discontinuity in the transport properties when seen in terms of potential temperature.

1 Introduction

The Asian monsoon is the most active convective region during boreal summer and, as such, is also the largest provider of air ascending from the tropospheric boundary layer to the upper troposphere and the lower stratosphere. Usually the air

does not ascend directly into the stratosphere but convective air is mostly detrained below the tropopause within the tropical tropopause layer (TTL) and is subsequently carried aloft by slow motion (Fueglistaler et al., 2009) . The bulk of the convective detrainment occurs at about 200 hPa or 350 K (12-13 km) and is associated with the divergent upper component of the Hadley circulation (Garny and Randel, 2013). At such altitudes, radiative cooling dominates and the vertical motion is almost everywhere descending except within the clouds~~, due to a dominating radiative cooling~~. It is only at about 355-360 K (14-15km), depending on the location, that the mean clear sky radiative cooling leaves room ~~to~~ for warming (McFarlane et al., 2007). As the ~~short wave~~ short-wave absorption is very small~~at such levels, this~~ , the reversal is mainly a ~~long wave effect which is~~ long-wave effect due to the very cold temperature at the tropopause, such that the absorption of upward long-wave radiation exceeds the emission. This cold temperature is maintained by the adiabatic cooling of the air which is pumped across the tropopause and ~~entering~~ enters the Brewer-Dobson circulation (Randel et al., 2007; Randel and Jensen, 2013). The radiative effect of clouds ~~in~~ on their environment provides a ~~cooling or warming~~ perturbation that can, ~~accordingly~~according to its sign, rise or lower ~~locally the~~ the local mean all sky level of zero radiative heating (LZRH) (Yang et al., 2010; Wright and Fueglistaler, 2013; Berry and Mace, 2014; Johansson et al., 2015). As ~~this~~ the LZRH plays the role of a repelling transport barrier, a question is whether it forbids air parcels detrained below to reach levels above. ~~It was proposed (Corti et al., 2006) that~~ Corti et al. (2006) proposed that fluctuations in the radiative heating provided by cirrus clouds may help ~~parcel~~ parcels to cross the LZRH. However, Tissier and Legras (2016) found that this seldom happens and that convective sources of air reaching the tropopause are for 80% located above the LZRH.

During the Asian monsoon, a wide anticyclonic circulation denoted as the Asian Monsoon Anticyclone (AMA) sits over the ~~lower layer~~ quasi-stationary low pressure centre in the lower layers. This circulation, which reaches its maximum intensity near 360 K, ventilates the top of the monsoon convective clouds and redistributes the detrained air over a large area. Satellite observations show that tropospheric compounds emitted at the surface, like CO, and aerosols generated from these compounds, tend to concentrate within the AMA while it is depleted in stratospheric borne ozone (Randel and Park, 2006; Park et al., 2008; Randel et al., 2010; Vernier et al., 2015; Santee et al., 2017; Luo et al., 2018). These observations have been corroborated by a number of numerical simulations based on Lagrangian or general circulation models which all show confinement of tropospheric tracers within the AMA ~~(James et al., 2008; Park et al., 2009; Tzella and Legras, 2011; Wright et al., 2011; Bergman et al., 2012, 2013; O~~ There is, however, a ~~dispersion in~~ lack of consensus on the interpretation of what is actually observed. Basically, some studies support that the ascent of air within the AMA, in the clouds and above the clouds, ~~canalize~~ canalizes the flow from the troposphere to the stratosphere in a sort of isolated chimney with a core above the Tibetan ~~plateau~~Plateau. This upward flow would be then redistributed horizontally at the top of the chimney, corresponding approximately to the tropopause level above the Tibetan ~~plateau~~ Plateau (Bergman et al., 2013; Pan et al., 2016; Ploeger et al., 2017). Other studies see a broader spiralling ascent and stress that only a limited part of the ascending flux is processed within the AMA and that a large flux, mostly of maritime origin, finds its way to the stratosphere by circulating around the AMA ~~but~~ without penetrating its core (Orbe et al., 2015; Tissier and Legras, 2016; Fan et al., 2017; Vogel et al., 2019). It has been discussed that some of these discrepancies can be due to the differences between the ~~reanalized~~ reanalysed winds, vertical velocities and heating rates which are quite

different among available ~~reanalysis~~reanalyses, being notoriously large between ERA-Interim/IFS and MERRA-2/GEOS5, the most used by modellers, in the Asian monsoon region (Tegtmeier et al., 2019).

The goal of this work is to seize the opportunity of the release of the ERA5 by the European Centre of Medium Range Weather Forecast (ECMWF), a new generation reanalysis incorporating very recent progresses in numerical weather forecast, to revisit this problem in a systematic and quantitative way. In addition, we use state of the art diagnostics of the heights of convective clouds from high frequency and high resolution geostationary observations. We also focus on reconciling previous studies ~~by~~ and on providing a simple quantitative account of the modelled transport across the TTL with a 1D model of transport with losses.

Section 2 describes the data and methods used in this study. Section 3 presents the results of the extensive 3D Lagrangian calculations. Section 4 discusses how a simple 1D model can reproduce the properties of the 3D transport across the TTL. Section 5 offers discussion and conclusion. Complementary results and discussions can be found in the Supplement.

2 Data and methods

2.1 ECMWF ~~reanalysis~~reanalyses

We compare here the two ~~reanalysis~~ reanalyses ERA-Interim and ERA5 of the ECMWF. The ERA-Interim was initially made available at the end of 2007. It is based on the Cy31r2 version of the Integrated Forecast System (IFS), released in 2006, with T255L spectral resolution and 60 hybrid levels up to 0.1 hPa (Dee et al., 2011). It uses a 4D-Var assimilation with a 12h cycle. The ERA5 reanalysis ~~(Copernicus Climate Change Service, 2017)~~ (Copernicus Climate Change Service, 2017; Hersbach et al., 2019) was initially made available at the end of 2017. It is based on the C41r2 version of the IFS model with ~~T1367~~ T699L spectral resolution and 137 hybrid levels up to 0.01 hPa. It uses an ensemble 4D-Var assimilation with a 12h cycle. Between 155 and 65 hPa, the number of hybrid levels has changed from 6 to 17, providing a much better vertical resolution ~~in the region of the atmosphere relevant to this study~~of the TTL. The IFS has undergone many changes between ERA-Interim and ERA5, in particular regarding the parametrization of cloud processes.

We use ERA-Interim winds, temperature and ~~diabatic~~ radiative heating rates on the ~~hybrid levels of the model~~ model hybrid levels at a 1° horizontal resolution in latitude and longitude over the sphere. Winds ~~are available from both the analysis and the forecast while heating rates are a pure forecast product. The data~~ and temperature are available 3-hourly by ~~interspelling~~ interleaving the 3h and 9h forecasts with the ~~analysis available every~~ 0h and 6h analyses during each 12h assimilation cycle. Radiative heating rates, produced by the forecast, are available 3-hourly. We use ERA5 winds, temperature and ~~diabatic~~ radiative heating rates on the ~~hybrid levels of the model~~ model hybrid levels at a 0.25°horizontal resolution in latitude and longitude ~~within the FullAMA domain bounded by 10W and 160E in longitude and 0 and 50N in latitude. See more details about this choice in Sect~~over the domain described in Sec. 2.3. The data are available hourly from analysis (winds and temperature) and forecasts (heating rates). Notice that in both ERA-Interim and ERA-5, the winds and temperature are ~~available as~~ instantaneous fields while the radiative ~~heating are~~ heatings are accumulations over, respectively, ~~3-hourly and hourly accumulations~~3h and 1h. The heating rates are treated as centred with a time shift with respect

to winds and temperature, of 1h30 in the ERA-Interim and 0h30 in the ERA5. The vertical shift of the vertical velocities with respect to the other variables in the IFS is also accounted.

~~Significant differences~~ The ERA-Interim and the ERA5 differ significantly in the cloud properties over the Asian monsoon region ~~are visible between ERA-Interim and ERA5 as documented in Tegtmeier et al. (2019)~~(Tegtmeier et al., 2019). The maximum cloud cover occurs at a lower level in the ~~ERA-Interim~~ ERA5 than in the ~~ERA5~~ ERA-Interim and is smaller. The ERA5, however, exhibits more high penetrative convection than the ERA-Interim, especially over the Tibetan ~~plateau~~ Plateau (Tegtmeier et al., 2019) and more activity at better resolved small scales in general (Hoffmann et al., 2019). Fig.1 shows the ~~resulting~~ cloud radiative heating (CRH), defined as the difference between the all-sky and the clear-sky radiative heating, for both reanalyses in the monsoon region ~~for both reanalysis. The CRH is located lower in altitude for~~ . The cloud radiative heating is exerted at lower altitude in the ERA5 and therefore disturbs less the clear sky LZRH ~~on a less extended region than for~~ from its clear sky value than in the ERA-Interim. ~~It can be shown that the~~ The ERA5 cloud disturbance of the LZRH concentrates over land and in particular over the Tibetan ~~plateau~~ Plateau which corresponds to the largest lobe in the green curve. ~~On the overall the~~ Tegtmeier et al. (2019) found that the all sky ERA5 ~~heating rate are the more~~ radiative heating rates are the most consistent with estimates based on active satellite measurements of the cloud vertical distribution (Berry and Mace, 2014; Johansson et al., 2015) ~~as shown in Tegtmeier et al. (2019)~~ when compared with four other ~~reanalysis~~reanalyses .

2.2 Lagrangian trajectories

Lagrangian trajectories are calculated using the Lagrangian model TRACZILLA (Pisso and Legras, 2008), which is a variation of FLEXPART (Stohl et al., 2005). TRACZILLA interpolates velocities and heating ~~rate~~ rates directly from the hybrid grid to the location of the parcel using ~~log pressure interpolation or potential temperature interpolation in the vertical. The nominal vertical coordinate can be log pressure for kinematic calculations using vertical velocities~~ vertical log pressure interpolation for kinematic trajectories or potential temperature ~~for diabatic calculations using radiative heating rates~~interpolation for diabatic trajectories. The time step is 7.5 minutes. In both cases, temperature and pressure are calculated along the trajectory. As the trajectories are intended to wander ~~outside of~~ at high altitude outside the clouds, the diabatic ~~calculation use the total radiative heating rate but discard the latent heating as well as the vertical heat diffusion, the latter being generally negligible in the region of interest~~calculations use only the all-sky radiative heating rates. The kinematic calculations use the total vertical ~~velocity~~ velocities that includes the net convective flux, ~~that~~ which cannot be separated. This set-up is ~~quite~~ similar to that of ~~, e.g.,~~ Bergman et al. (2013). Some other studies where the tracers are initialized in the boundary layer used instead the total heating rate ~~(Vogel et al., 2015; Ploeger et al., 2017; Vogel et al., 2019; Li et al., 2019). Above~~ (Vogel et al., 2015, 2019; Li et al., 2019). As the altitude rises above the level of maximum cloud cover, the total heating rate converges rapidly to the radiative heating rate~~as a function of increasing potential temperature~~. Experiments made using total diabatic heating (not shown) do not change our results.

2.3 Domain

~~Observations show that there is a strong correlation in averaged maps between the geopotential or Montgomery potential contours and tracer contours (Park et al., 2007, 2009), showing the confinement properties of the AMA~~The confinement properties of the AMA are easily established from the strong correlation of time-averaged maps of tropospheric tracers and the AMA mean circulation (Park et al., 2007, 2009; Randel et al., 2010). The mean Montgomery potential ~~for several levels during Summer 2017~~ is shown in Fig. S2 of the Supplement ~~.~~ on several isentropic levels and defines the extent of the AMA during summer 2017. However, the AMA fluctuates a lot from day to day and it is ~~much more~~ very difficult to define an operational boundary on instantaneous maps. Ploeger et al. (2015) use the gradient of potential vorticity to mark the boundary of the AMA but ~~very often~~ this boundary is ~~fuzzy with~~ very often fuzzy and broken into numerous patches. We avoid this problem by considering a domain, denoted as FullAMA, that is intended to encompass the AMA and reveals its confinement properties but, at the same time, to be small enough such that trajectories leaving the AMA also leave the domain very shortly after. The FullAMA domain is bounded in longitude by 10°W and 160°E and in latitude by 0°N and 50°N. This choice is also dictated by practical considerations as it is very costly to manage calculations using the ERA5 at full resolution in the global domain.

Therefore, the ERA5 calculations are conducted within the FullAMA domain, all trajectories reaching its boundary being discarded~~while~~ . For the sake of comparison, the ERA-Interim calculations are conducted both in the global domain and the FullAMA domain~~(~~, the latter configuration being obtained by clipping the global trajectories ~~who leaves FullAMA) for the sake of comparison~~which leave FullAMA. In addition, all trajectories reaching the 30 hPa or 500 hPa surfaces are discarded since parcels then exit the vertical region of interest. The global ~~calculations~~ trajectories of the ERA-Interim are also exploited to study the impact of the monsoon at planetary scale.

~~A second restricted domain, the AMACore, is defined to fit the region of closed streamlines in the Montgomery potential shown in Fig. S2. This domain is bound by 10E and 140E in longitude and by 10N and 40N in latitude. It spans the core of the AMA circulation.~~

2.4 Cloud data and trajectory sources

We characterize cloud tops using the SAF-NWC (Eumetsat ~~Satellitte~~ Satellite Application Facility for Nowcasting) software package (Derrien and Le Gléau, 2010; Sèze et al., 2015) that determines cloud type and cloud top height from geostationary satellites using visible and infra-red channels. The 2016 version of the SAF-NWC package has been applied to the MSG1 (Meteosat 8) and Himawari satellites ~~at full spatial resolution~~ with 15 ~~'~~ minutes sampling for MSG1 and 20 ~~'~~ minutes sampling for Himawari during June-July-August 2017. MSG1 is used west of 90°E and Himawari east of this longitude. The auxiliary temperature profiles are provided from the ERA5 at hourly temporal resolution and 32 pressure levels, as well as the altitude and the temperature of the thermal tropopause. The cloud data at full spatial resolution are projected onto a regular grid in the ~~AMA~~ FullAMA domain with spatial resolution 0.1° in both longitude and latitude using the closest neighbour method. The data are updated on this grid ~~are updated~~ every 5 minutes to the most recent satellite data. When a satellite image is missing, the gap is filled by the last ~~one~~ image available for this satellite. The SAF-NWC package uses an ensemble of retrieval algorithms choosing the best one for each pixel according to a selection tree. See Bucci et al. (2019) for a more detailed account of the ~~algorithm~~method. Depending on the retrieval path, the cloud top pressure can be determined among a continuous range or

within a set of discrete values. In particular, a small number of single pixel cloud tops are found at 100 and 70 hPa. We have not filtered these values as they are found at the core of very high and cold systems and are liable to capture overshooting events. No convective clouds are considered outside of the FullAMA domain.

In forward runs, cloud tops are used to initialize trajectories every hour over the period June-July-August 2017 by selecting high clouds in the FullAMA domain~~at that time: we retain all clouds~~. We retain all cloud pixels above 250 hPa within high~~and~~, very high opaque and thick semi-transparent types as per the SAF-NWC classification. For each of ~~these~~ the selected cloud pixels, a new trajectory is launched at its top and is integrated forward in time for ~~up to 2~~ two months. Notice that a large number of mid-level clouds which are associated with heavy monsoon precipitations escape this selection.

~~Parcels are launched hourly from the top of the clouds over the period June-August 2017. On the overall 308 millions trajectories have been launched during this period.~~ Four separate integrations of two months are performed. The first two uses the ERA5 dataset and are bounded within the FullAMA domain. In the sequel, the diabatic version is labelled EAD and the kinematic version is ~~labeled EAZThe last~~ labelled EAZ. The additional two integrations are performed using the ERA-Interim dataset and the trajectories are integrated within the global domain. The diabatic version is labelled EID and the kinematic version is labelled EIZ. On the overall, 1.2 billions trajectories are launched during summer 2017.

In backward runs, the trajectories are initiated on a one degree grid at selected potential temperature and are launched every 15 minutes in the FullAMA domain, and every hour in the global domain for July-August-September 2017. The trajectories are integrated backward for up to two months when they do not exit the domain. The trajectories are then processed to find encounters with clouds. This is done, for each parcel, from 6-hourly outputs by interpolating the parcel position every 5 minutes and comparing the parcel pressure with that of the cloud tops from the SAF-NWC image at 0.1° resolution which is valid at that time~~(and renewed every 15' or 20')~~. When a cloud top with lower pressure than the parcel is found at the same location, the backward trajectory is flagged as ending there. ~~Due to flaws in the retrieval, 24 images have been blacklisted during Summer 2017 and removed from the processing.~~

2.5 Convective impact

The effect of the transport of ~~monsooon~~ monsoon convective parcels in forward calculations is measured as the convective impact. Basically, we divide the tropical atmosphere into cells of width $D = 1^\circ$ in latitude-longitude and of height $\Delta\theta = 5$ K. We then count the number of convective parcels found within ~~this~~ each cell over the full two months of integration. This count can be performed in the *target space*, that is at the location of the parcels when they are sampled along their trajectories, or in the *source space*, that is at the location of the parcels when they are released. In the latter case, the parcels are ~~further stratified according to the potential temperature of the parcels~~ sorted according to their potential temperature in the target space. In order to be independent of the arbitrary discretization, the convective impact is weighted for each convective parcel by $\tau\delta^2\cos(\phi_S)$ where τ is the time interval between two satellite images (1 hour), δ is the size of the pixel in the satellite image (0.1°) and ϕ_S is the latitude of the convective source. In the target space, the count is further multiplied by the sampling interval along the trajectory $\Delta t = 6$ hours and is normalized by the mesh size in the target space that is $\Delta\theta D^2\cos(\phi_T)$ where ϕ_T is the mean latitude of the target cell. Hence the full normalization factor for the impact ~~density~~ in the target domain

is ~~$\tau \Delta t \delta^2 \cos(\phi_S) / \Delta\theta^2 D^2 \cos(\phi_T)$~~ $\tau \Delta t \delta^2 \cos(\phi_S) / \Delta\theta D^2 \cos(\phi_T)$. The resulting quantity is called the ~~impact density~~*impact density*. In the source domain, ϕ_T is replaced by ϕ_S in the denominator and therefore the cosine factors disappear. The resulting quantity is called the ~~source density~~*source density*. We define the ~~cumulated impact~~ *cumulated impact* as the integral of the ~~convective~~ impact density over the FullAMA domain for a given level. A convenient unit for the impact density is $\mathrm{day}^2\mathrm{K}^{-1}$ and we use $\mathrm{day}^2\mathrm{km}^2\mathrm{K}^{-1}$ for the cumulated impact

As the impact density and the ~~sourced~~ source density vary considerably with altitude, it is ~~also~~ useful to define an equalized quantity for the sake of comparison. ~~This equalized quantity within a given domain~~ The *equalized impact* is defined , for each ~~pixel~~cell within a given domain, as the ratio of the impact ~~with respect~~ density to the value obtained by redistributing equally the cumulative impact over all ~~pixels~~cells, according to their area.

~~Notice~~ We stress that each forward parcel is allowed to be counted as many times as it appears within the domain in the 6-hourly outputs during the integration period.

~~The impact can also be stratified according to the age, that is the time elapsed from the parcel release at the top of a convective cloud until its sampling. The cloud top distribution is equivalent to the impact at age 0.~~

~~The~~ backward trajectories are analysed according to the probability of hitting a convective cloud within the integration time or exiting the FullAMA domain. The sources are counted on a mesh of ~~one degree~~ 1° resolution in the horizontal and 1 K in the vertical. They are normalized and equalized in the same way as the forward sources. ~~In~~ An important difference with respect to the forward case is that in the backward analysis, only the first hit is accounted.

The impact is not meant to be an estimate of the convective mass flux or the mixing ratio of convective air since we do not have, in the present state of the art, any information on the mass detrainment at the top of the observed clouds. It should be seen at a metric for convective influence which can be used to study how parcels originated from convection are confined, dispersed or diluted in the TTL.

3 Results

3.1 Impact overview

We first present an overview of the impact in order to justify our approach. We use the ERA-Interim ~~calculations~~ diabatic trajectories (EID) to compare calculations made in the global domain and in the restricted FullAMA domain. Figure 2 shows the ~~accumulated convective impact~~ impact density on the 380 K surface for parcels launched from the cloud tops over the period ~~1 June 2017 to~~ 1st June - 31 August 2017 ~~with forward integration~~ and integrated forward for two months. The ~~air masses confinement~~ confinement of air masses inside the AMA is clearly visible and exhibits similar patterns in both the FullAMA and the global domain ~~calculations for the ERA-Interim diabatic version~~ versions of EID (panels a & c). Over the FullAMA domain, ~~the correlation between the impacts~~ Figure 3 shows that the correlation of the impact at 380 K ~~in the two panels~~ between these two versions is 94.3% and on the average is 96.9% between 340 K and 420 K (~~see Fig. 3~~black solid curve). The ratio between the maximum impact ~~for an integration restricted to the FullAMA domain, in panel~~ in Figure 2(a) ~~, and the maximum impact in the FullAMA box for an integration in the global domain, in panel~~ and Figure 2(c), is 0.91~~at~~

380 . It . This ratio decays from 1 at 350 K to 0.8 at 420 K (red solid curve in Fig. 3). Similarly, the ratio of the cumulated impacts over the FullAMA domain is 0.6 at 380 K and decays from 0.88 at 350 K to 0.52 at 420 K (blue solid curve in Fig. 3). At the same time, the total cumulated impact itself (shown in Fig. 4) decays by a factor 18 in the global calculation and 30 in the FullAMA calculationscalculation. The differences between the two calculations are due to parcels that leave the domain and disappear in the FullAMA calculations while re-entering calculation while they re-enter the FullAMA domain in the global calculationscalculation. However, these parcels seldom re-enter the AMA core, hence the difference between the ratios of the maxima and of the cumulated impacts. As altitude rises, the cumulated impact decays strongly as a result of dynamical erosion of the AMA and this decay is much larger than the variation of the impact ratio between the global and the FullAMA calculations. Therefore we The reentering parcels have travelled over long loops or even a full latitude circle and have been carried within filamentary structures submitted to strain and stretching resulting in mixing with the environment. Therefore, it is arguable to count them within the background rather than being part of the convective parcels when they reenter the FullAMA domain. We conclude that the confinement seen in the FullAMA calculations is not an effect of the boundaries and we will focus on this domain in most of the sequel. Further comparisons between the FullAMA and the global domain are made in Sect. S7 of the Supplement .

Figure 2 also shows the FullAMA impact for the ERA5 diabatic calculations trajectories (panel e). The pattern is again very similar to that of the ERA-Interim calculations trajectories in the panel (a) with a correlation of 99%, but the maximum impact ratio and the cumulated impact ratio are, respectively, reduced by a ratio 0.44 and 0.46. These results are due to the fact that obtained because the horizontal distribution of the impact depends essentially of the horizontal isentropic circulation which seldom differs between ERA-Interim and ERA5 while the amplitude ratio depends ratios depend on the vertical motion which differs a lot over the whole column as shown in Fig. 3 (dash curves).

Finally, Figure 2 shows the source density of convective parcels reaching the 380 K surface (panels b,d,f). The largest contribution in the FullAMA ERA-Interim calculations trajectories (panel b) comes arises from North India (mostly the Gange valley, Bengal and the north of the Bay of Bengal), with two other spots over the south of the Tibetan plateau Plateau and in South China. These areas are surrounded by a wide halo of sources mainly over the Asian continent but with some significant component over the Sea of China and the Pacific east of the Philippines. The distribution of the global sources (panel d) exhibits a general intensification, by about a factor 2, without changing the pattern of continental sources but also a shift towards a larger share of the maritime sources, that are much more intense relatively relative to the continental sources. The corresponding trajectories are travelling trajectories from maritime sources extend along the easterlies in the southern branch of the AMA and mostly leave the FullAMA domain without recirculating around or entering the AMA core.

The source distribution for the ERA5 is similar to that of the ERA-Interim but with important differences. The distribution is much more concentrated on the Gange valley and the Tibetan plateau Plateau with weakened contributions from Bengal and South China. The reinforcement of the Tibetan plateau is directly linked to the high penetrative convection above the plateau which is mentioned above in Sec. 2.1.

The source distribution shows a relative minimum over the narrow region which corresponds to the steep southern slope of the Himalayan plateau. The monsoon flow hitting this slope generates a lot of precipitations but does not lead to high convective

towers that penetrate the TTL. ~~This is not a feature of the 2017 season only but shows up also in a multi-year climatology of the high clouds (not shown).~~ More generally, other areas providing a lot of monsoon precipitations like the Ghats in South India or the Arakan mountains are not visible in our source maps.

3.2 Vertical transport and erosion

~~Figure 4 upper panel~~ The upper panel of Fig. 4 shows the cumulated impact for the four FullAMA experiments (EAD, EAZ, EID, EIZ) compared to the high cloud distribution which is ~~also the impact at age 0. The high cloud distribution in the FullAMA domain is the same~~ the common initiation for all experiments~~; it peaks strongly~~ . The cloud distribution strongly peaks at $\theta = 349.5$ K and is mostly distributed between 340 K and 370 K. Some rare convective events, however, are still found up to about 400 K in the stratosphere while the applied 250 hPa selection threshold produces a ~~rapid cutoff~~ cut-off in the lower layers below 335 K. The cumulated convective impact in the FullAMA domain peaks near the cloud peak. The ~~maximum value of the impact distribution~~ peak is located lower by a few degrees ~~in potential temperature~~ for the diabatic trajectories (solid) than for the kinematic trajectories ~~and the cumulated~~ (dash) and the total impact below the cloud peak is also larger. The ~~smallest peak for EID is~~ EID impact curve (solid red) exhibits the smallest maximum and is also associated with the smallest slope ~~of the impact~~ above the source peak~~and indicates~~ , indicating that this case corresponds to the fastest upward transport. On the opposite, the ~~largest peak for EIZ is associated with~~ EIZ impact curve (dash red) exhibits a large maximum and the largest slope. The two ERA5 ~~distributions exhibit intermediate results~~cases (blue) exhibit intermediate and similar slopes. We already see here, as it ~~will be confirmed later~~is confirmed below, that EID and EIZ calculations exhibit large differences and bracket the two ~~ERA-5~~ ERA5 calculations which are much closer. ~~Figure 4 right panel~~ The lower panel of Fig. 4 shows the distribution of the clouds together with the vertical profile of the heating rate, here reduced to the ~~core AMA~~ restricted domain (20°E-140°E and 10°N-40°N) ~~, avoiding the boundaries~~ which avoids the frontiers of the FullAMA domain. ~~It is visible~~ We see that the zero level of radiative heating ~~occurs~~ is above the maximum level of the sources, in a range of altitudes where the ~~source density decays approximately exponentially with the~~ cloud density basically decays exponentially with potential temperature. The straight ~~fit line shown in the figure~~ line in the panel corresponds to a decrement rate ~~of 0.325~~ $\beta = 0.325$ K^{-1}. As the ERA-Interim all sky heating crosses the zero axis at a lower altitude than ERA5 and provides stronger heating above 370 K, the ERA-Interim impact is expected to be stronger and to propagate faster upwards, as observed.

We now define the age of a parcel as the duration elapsed from its release by convection. Figure 5 shows how the convective impact propagates inside the ~~AMA~~ FullAMA domain from the sources as a function of age. In both the kinematic and diabatic cases, the dispersion occurs ~~both~~ upward and downward. A clear separation occurs in the diabatic cases between the ascending and the descending ~~branch~~branches, transporting parcels away from the main source level. The descending diabatic ~~branch is~~ branches are very intense, ending at the imposed ~~cutoff~~ cut-off level. The upper ~~branch exhibits~~ branches exhibit a strong attenuation due to parcels exiting through the lateral boundaries, leading to the ~~fast~~ strong decay of the impact with altitude seen in Fig 4. The ~~vertical~~ upward propagation is the slowest for EIZ and the fastest for EID with the two ~~ERA-5~~ ERA5 cases in between and fairly close together. The propagation is estimated by fitting a straight line to the crests of the distribution on each isentropic layer. See also Sec. S4 ~~in~~ of the Supplement. The slope, denoted as A in the sequel, is found to be 1.08, 1.11,

0.97 and 1.35 $\mathrm{K\,day^{-1}}$ for, respectively, EAZ, EAD, EIZ and EID. ~~These~~ For diabatic cases, these values are consistent with the average heating rates of ERA5 and ~~ERA-I~~ ERA-Interim above 370 K (see Fig. 4)~~above 370~~. It is shown in Sec. ~~S9 of the Supplement~~ 4 that this result is expected when diffusive transport by heating rate fluctuations can be neglected. The descending branch of the diabatic impact and the withdrawal of parcels from around the 350 K level is also consistent with the heating rate crossing from cooling to warming near this level in both ~~reanalysis~~reanalyses. The close proximity of the zero level of heating rate and of the maximum ~~detrainement~~ detrainment of the clouds is not fortuitous but can be seen as a manifestation of the Fixed Anvil Temperature principle (Hartmann and Larson, 2002).

~~As~~ Even if the vertical velocities are ascending everywhere in the monsoon region, the ~~descending branch of the kinematic experiments which is quite clear in~~ kinematic distributions in the two left panels of Fig. 5 ~~must is located in another region~~exhibit a clear descending branch. The descent ~~occurs~~ does not occur within the monsoon region but as a result of the ~~horizontal westward transport of~~ westward horizontal transport by the AMA that brings the convective ~~parcel~~ parcels over the Arabian desert and the Sahara where the ~~air~~ vertical motion is subsiding (see Sec. S5 of the Supplement). This transport is one of the branches of the Hadley-Walker circulation during the monsoon season. ~~The other branch that connect to the southern hemisphere is only implicit here but can be seen in the global experiments (see Sec. S7 of the Supplement).~~

As we see in the next section, it is also produced by the diabatic circulation. The large differences between kinematic and diabatic trajectories transport properties in the ERA-Interim and the fast vertical transport of its diabatic version have already been noticed in a number of previous studies ~~(e.g., Bergman et al., 2015; Bucci et al., 2019; Li et al., 2019)~~(e.g., Ploeger et al., 2012; Bergman e

~~Notice that the commonly used metric of the mean age might hinder the differences in vertical propagation. Figure ?? shows the normalized impact spectra taken from Fig. 5 at three vertical levels in the upper branch. The different separations of the modal peaks reproduce the differences in vertical propagation. However, the widening of the distributions is asymmetric and varies largely. The fastest propagation by EAD is associated by a narrow dispersion while the slowest propagation by EID is associated with a broad dispersion, the result being that the mean age separation, that is the mean age slope with altitude, is almost the same. The propagation and the dispersion in the ERA5 case are intermediate and the mean age slope remain close to the ERA-Interim value. This property is probably fortuitous and shows that the mean age metric is not reliable to estimate transport properties. We discuss below this observed behaviour and the possible reasons of the differences in Sec. 4 within the framework of a simple 1D model.~~

Figure 6 shows the decay of the total impact integrated over ~~three isentropic layers~~ the FullAMA domain and three vertical layers (defined in the caption) as a function of age. At small ages, the impact is confined in the mid-layer, where the sources ~~concentrates. Then~~concentrate. Then, the upper and lower layer impacts grow, ~~the latter being~~ and the latter is rapidly dissipated by the bottom cut-off, so that eventually the upper layer impact dominates. The decay of the lower and mid layer impacts is much faster in the diabatic cases due to the descending motion within the source region. The asymptotic decay time scale α of the upper layer is quite similar among EAD, EAZ and EID. It is larger for EIZ but the asymptotic limit, where the upper layer dominates, is only marginally reached in that case. We retain the value for ERA5 diabatic, that is $\alpha = 13.3\,\mathrm{day}$ as the erosion ~~rate~~ time-scale of the upper-layer. This time scale is of the order or smaller than the mean circulation rate in the AMA, two to three weeks, as found in Sec. S2 of the Supplement. Therefore the AMA exhibits only weak confinement properties. If we

assume that this erosion rate and the mean vertical ascent A explain the dilution of the impact with altitude, we get a decay rate ~~$(\alpha A)^{-1} = 0.69$ K^{-1}~~ $(\alpha A)^{-1} = 0.068$ K^{-1} very close to the value ~~0.65~~0.065 K^{-1} obtained from Fig. 4.

In the sequel, we will focus on the ERA5 diabatic ~~calculations.~~ trajectories This set-up is shown to be the most relevant to interpret the airborne data of the StratoClim campaign by Bucci et al. (2019) and it produces results very close to the kinematic set-up as far as the upper branch of transport from the convective sources is concerned. More comparisons between diabatic and kinematic ~~calculations~~ trajectories and between FullAMA and global ~~calculations~~ trajectories can be found in the Supplement.

3.3 Horizontal distribution of impact and sources

In order to ~~display~~ investigate how the confinement varies with altitude, Fig. 7 shows the impact distribution for four ~~layer~~ layers from 340 K to 370 K in the ERA5 diabatic calculations. In the lowest layers at 340 K and 350 K (panels a and c), the convective parcels are rapidly expelled to other regions by the divergent motion which is maximum at these levels (see Fig. S4 of the Supplement) and to lower levels by diabatic cooling. Due to this combined effect, the impact ~~is maximum~~ at 340 K is maximum west of the monsoon region over the Arabian desert and the Sahara where the air is slowly subsiding. This upper circulation from the monsoon uplift region is one of the main branches of the Hadley-Walker circulation during summer. Other descent regions in the ~~southern hemisphere appear for global trajectory simulations~~ Southern Hemisphere, corresponding to the other branches, appear for global trajectories (see Fig. S10 of the Supplement). We stress that the descent branches are also observed for kinematic ~~calculations~~trajectories, as seen in Figs. S8 and S10. However, as vertical velocities are positive over the whole tropospheric column in the monsoon region, the total descending impact is reduced with respect to the diabatic simulations. The distribution of sources for the 340 K and 350 K levels (see Fig. 7(b,d)) has a large maritime contribution, in particular over the Bay of Bengal (BoB), and the continental contribution concentrates over India in the eastern regions adjacent to the BoB.

A ~~change~~ drastic change in the pattern occurs at 360 K with ~~an impact pattern~~ the impact now centred over continental Asia (see Fig. 7(e)) and a distribution of the sources ~~that concentrates over North Inda~~ concentrated over North India and the Tibetan ~~plateau~~ Plateau with maritime sources only on the North of the BoB (see Fig. 7(f)).

Figure 7(g,h) and Fig. 8 show that between 370 K and 420 K, the pattern remains basically constant both for the target impact and for the sources, but for the exponential dilution shown in the upper panel of Fig.4, which is fully explained above as the combination of constant loss with uniform ascent over the AMA. ~~The target pattern quite closely follows~~ It is remarkable that the impact pattern, in spite of the dilation due to pressure drop (that cannot occur in the vertical because of the quasi-constant ascent rate), does not exhibit any expansion with height and rather shows a columnar shape. The target impact contours closely follow the contours of the Montgomery potential (see also Fig S2) that describes the main circulation within the domain.

The self similar behaviour of the forward impact is confirmed by the backward trajectories. Fig. 9 is produced from the backward EAD trajectories for the three months July-August-September 2017 within the FullAMA domain. The percentage of convective hits reaches 100% at 360K within a large region at the ~~center~~ centre of panel (a). This percentage decreases with altitude but remain high, with values above 80%, up to 380 K~~. At~~, and up to 50% in the AMA core at 400 K ~~, a large majority of parcels leaves~~ while the overall shape remains the same at all levels. The region of high percentage of convective

hits is surrounded by a periphery which is almost entirely filled with background air that came across the boundary of the FullAMA domain~~before reaching convection~~. Figure 9 also shows the source distribution in the horizontal and in the vertical. The parcels released at 360 K reach convection in a close neighbour of this level (panel c) and they show a mixed distribution of sources over the maritime and continental regions (panel b) like in Fig 7(f). For parcels released at higher levels the vertical distribution of sources broadens from near 360 K to the level of release (panels f, i, l). The distribution tends to peak near 365 K and is skewed with a sharp ~~cutoff~~ cut-off on the lower side and a longer tail on its upper side. The secondary peaks seen in the 380 K and 400 K distribution result from the discrete cloud top values produced by the SAF-NWC retrieval. The intensity of this peak at 400 K is an indication that rare events of penetrative convection might make a significant contribution to the impact in the lower stratosphere. A better assessment of this penetrative convection is clearly needed to substantiate this finding. This is a challenge for present and future geostationary observations at high spatial and temporal resolution. The patterns of the horizontal distribution (panels e, h, k) are showing the same concentration of sources in North India and the Tibetan Plateau as for the forward case in Fig.4 with a decreasing contribution of over sources as the altitude rises. This localization of the convective sources for parcels reaching the top of the TTL was already observed, using backward trajectories, by Bergman et al. (2013) and attributed to the existence of a narrow conduit from the ground to the tropopause. We see here that the narrow conduit is that of convective towers bringing air from the boundary layer to the top of the clouds but that it stops there and that subsequent motion is distributed over a much wider area.

It is useful to compare the backward hit percentage and the forward impact. If we consider the two levels 380 K and 400 K, the areas of backward hit percentage larger than 70% for the first and 30% for the second are fairly similar, 15.210^6 km^2 and 16.110^6 km^2 respectively, and cover a large portion of the AMA domain, whatever definition is used. This shows obviously that the convective influence propagates high in the lower stratosphere and that the in-mixing of background air is very limited. However, the ratios of the forward cumulated impact contained in these areas to that in the same areas at 355 K where it is maximum can also be calculated and are only 12% and 4,5% respectively. There is no paradox, it only means that air escapes easily from the AMA as it ascends but penetrates much less easily inside. The distribution of backward hit percentage is also compatible with the observation of an apparent plume of tropospheric tracer in the AMA which has been reported in several previous studies based on large scale data and large-scale models (Park et al., 2009; Randel et al., 2010; Pan et al., 2016, e.g.). A columnar AMA rich in parcels influenced by convection and surrounded by background air is producing this very pattern. Therefore we prove that observing such a tracer columnar pattern is not a proof of a chimney with impermeable walls as it is often assumed. It is generally known (see, e.g. Joseph and Legras, 2002) that forward trajectories link the stable structures at the initial point to the unstable structures at the final point in the future, while the backward trajectories link the stable structures at the initial point to the unstable structures at the final point in the past. Here the backward trajectories link the confined domain of the AMA to the LZRH surface, around which they tend to oscillate at long time while this same surface repels forward trajectories.

3.4 Age

~~In forward runs, the age of air is calculated as the time interval between the parcel release from the cloud tops and the crossing of a given θ level , multiple crossings being~~ In forward runs, the age of air at a given level and within a given cell is defined as the mean over all the parcels contributing to the impact at this level within this cell. The same parcel can be counted several times with different ages since multiple crossings are possible. In backward runs, the age of air is calculated as the time interval between the parcel release on the grid and the first hit of a convective cloud, and is averaged in the same way except that each parcel is counted only once. The forward age is shown in Fig. 10 for both the target and the sources. At 350 K, panel (c) shows a meridional split between air younger than one week in the South and older air in the North. The young region spans the easterly jet that carries rapidly the maritime air produced over the Bay of Bengal and the Sea of China to the West over Africa and outside of the FullAMA domain . At ~~340~~350 K (panel ~~a~~c), the age is 2 days or less where the impact concentrates south of the Bay of Bengal at very close proximity to the convective sources. The mean age is about 10 days over Sahara but much less over equatorial Africa. The age is larger in the ~~core AMA~~ AMA core region with a small impact due to the few parcels that recirculate within the AMA at this level. The pattern changes completely at 360 K (panel e) where a broad deep minimum age is seen at the core of the impact, surrounded by a region of larger age. The pattern persists at 380 K and 400 K (panels g and i) albeit with a ~~much~~ reduced contrast between the core and the periphery. Therefore, ~~we conclude that the impact concentration within the AMA core is not related to trajectories being trapped and with long residence times but to~~ the maximum impact density at the core of the AMA is maintained by the constant renewal by fresh convective air rising from below rather than by the trapping. This provides support to the "blower" hypothesis of Pan et al. (2016). However, we find that the AMA blows parcels away uniformly from 360 K and up, and not only above the tropopause.

The distribution of age in the source space shows that at the lowest levels 340 K and 350 K (see Fig. 10(b,d)) the age is maximum over the continental regions and minimum over the maritime regions~~due to the fact~~ . The reason is that the continental air circulates within the AMA before being expelled towards the major subsident regions over Arabia and Africa, while the maritime air is directly transported to these regions. At 360 K and above (see panels f,h,j), the mean age is fairly uniformly distributed over the whole sources, indicating no preference for a faster path from any region. ~~Similar results for the backward calculations are shown in~~ Sec. S8 of the Supplement shows that the age distribution of the backward trajectories agree very well with the forward distribution. Therefore we conclude that the age distribution indicates that the ascent occurs over a broad domain that covers the whole AMA rather than in a very localized region and that parcels remaining within the AMA spiral outward as they rise, as also found by Vogel et al. (2019).

3.5 Vertical crossover

In this section we concentrate on the domain where convection is the most active and relevant to the Asian monsoon. We divide this domain, labelled as Asia, into three subregions: Land, Ocean and Tibetan ~~plateau~~ Plateau as shown in Fig. 11. The Tibetan ~~plateau~~ Plateau is defined as the region with orography higher than 3800 m. We stress the need for a clear separation between ocean and land, that the commonly used rectangular boxes cannot provide. There are very noticeable differences, as shown in Tegtmeier et al. (2019), in reanalysis-based cloud properties and heating rates between the Bay of Bengal and the Sea of China on one side and the adjacent Indian subcontinent and South China on the other side.

Table 1 shows that the distribution of high clouds (as selected in Sec.2.4) favours the Ocean (68.4%) rather than the Land (26.6%) and the Tibetan ~~plateau~~ Plateau (5%). The maritime convection is ~~divided~~ further divided (not shown in the table) among the Sea of China and the Philippine Sea (23%), the West and Mid Pacific (17,1%), the Bay of Bengal (14%) and the Indian Ocean (10,8%). The land is further divided among the Indian Subcontinent (12.8%), Indochina (7.8%) and South China (6.4%). The maximum high cloud ~~covers lies on the the average~~ cover is located 4 to 6 K higher on the Land than on the Ocean, and up to 10 K higher over the Tibetan Plateau.

Table 1 also shows ~~the LZRH for ERA5 and ERA-Interim. In the ERA5 case, there is a separation of about~~ that the LZRH is everywhere 5 K ~~between the LZRH and the mean high cloud level, while for~~ above the maximum high cloud cover in the ERA5 while in the ERA-Interim ~~they are quite similar except over the Tibetan plateau where the LZRH remains higher by almost~~ the two levels are close over Land and Ocean but separate by 8 K over the Tibetan Plateau.

For the three regions and Asia as a whole, and for all source levels, we determine the proportion of trajectories, rising, descending or being stationary. In this purpose we divide the potential temperature range [322.5 K, 422.5 K] into 20 bins of width 5 K and we calculate, for each region, a 2D histogram for the source level and the mean level of the convective parcels during their life time. In the FullAMA calculations, this latter is the period of time between the launch and the exit of the FullAMA box, the exit through the lower cut-off or the end of the integration. In the global case, the exit occurs only through the lower cut-off. We then calculate the rising proportion, for each level, as the proportion of parcels borne in this level for which the mean ~~potential temperature along their trajectory~~ (life-time) level lies within bins ~~located above this level~~above it. Similarly the descending proportion is calculated for parcels with mean level below the initial level and the stationary proportion corresponds to parcels with mean level within the initial bin.

Figure 12, drawn for sources in the whole Asia region, shows a crossover at 362 K for both the FullAMA and global trajectories of EID. The crossover is located slightly above at 364 K for EAD, consistent with a smaller cloud radiative effect. At levels below the crossover, the two descent curves for EAD and EID within the FullAMA domain are very similar and drop rapidly due to the lower boundary. In the global domain, the drop is shifted to lower levels and delayed, due to ~~a better representation of the cross-hemisphere~~ the cross-hemispheric Hadley-Walker circulation. ~~The~~ This separation between ascending and descending motion near 360 K was already mentioned by Garny and Randel (2016).

Table 1 shows the crossovers for the three component regions. ~~Over Land and Ocean~~In the ERA5, the crossover is above the LZRH by ~~4~~5.8 K over ~~Land and 4~~Ocean and 3.4 K over ~~Ocean. This is not true over the Tibetan plateau where it is below by 2 for ERA5 and 3.5~~Land. It is below the LZRH by 1 K ~~for~~ over the Tibetan Plateau. The gaps are different but the ordering is the same for the ERA-Interim. ~~The crossover remains, however, very~~ Since the crossover of the Tibetan plateau is close to that of the neighbour ~~Land~~land, the only explanation is that parcels detrained above the Tibetan Plateau leave rapidly the area by horizontal motion to find regions of ascent.

The fraction of the high clouds that are above the crossover and therefore contribute to the upward transport is quite low. It is minimum over Ocean~~(~~, at 1.7% for ERA5~~)~~. The Land value is more than ~~double~~ twice larger (5.1%) and the Tibetan ~~plateau~~ Plateau further doubles it (10.8%). As the ERA-Interim crossover is lower, the corresponding proportions are about twice that

of ERA5. In both cases, continental convection is more likely than maritime convection to feed the upward motion above the LZRH and the Tibetan ~~plateau~~ Plateau is by far the most efficient region as already found by Tissier and Legras (2016).

As a result of the crossover pattern, and because maritime convection is more easily washed outside the FullAMA domain, the relative ~~contribution~~ contributions of Ocean and Land to the FullAMA impact at 380 K ~~is~~ are inverted with respect to the ~~proportion~~ proportions of high clouds in these regions (see Table 1). For the ERA5, the ratio Ocean/Land for the high cloud proportion is 2.57, and is 0.41 for the impact, therefore reduced by a ~~ratio~~ factor 0.16. This is partially explained by the ~~crossover~~ ratio of the high ~~clouds~~cloud crossover fractions, which is 0.33. The other explaining process is the washing out of the maritime impact. On the other side, the ratio Tibetan ~~plateau~~Plateau/Land is 0.19 for the high cloud and 0.41 for the impact. The enhancement by a ratio 2.2 is entirely explained by the ~~crossover~~ high cloud crossover fraction ratio which is 2.1. Similar numbers can be ~~found~~ derived for the ERA-Interim in the FullAMA domain. When we consider the global domain for the ERA-Interim, we see that the Ocean/Land impact ratio is 1.35, therefore a reduction by a ratio 0.52, slightly larger than the ~~crossover~~ high cloud crossover fraction ratio 0.4.

These results show that the enhanced impact of the Tibetan ~~plateau~~ Plateau is entirely due to the higher proportion of high clouds above the crossover in this region. The respective impact of oceanic versus land convection in the global domain is also mainly explained by this crossover proportion. There is more chance for parcels from continental convection to be trapped within the AMA but most of the air reaching the 380 K surface does not circulate first within the AMA. This result corroborates the findings of Tissier and Legras (2016) and Vogel et al. (2019).

4 A simple model of AMA confinement

In this section we investigate how the observed behaviour of the impact in the FullAMA region can be represented by a simple 1D model based on our observations. We consider a simple advection-diffusion model with loss for the impact $F(\theta,t)$:

$$\frac{\partial F}{\partial t}+\frac{\partial \dot{\theta} F}{\partial \theta}=-\alpha \frac{1}{\alpha} F+\kappa \frac{\partial^2 F}{\partial \theta^2}+S(\theta) \tag{1}$$

where α is the erosion ~~rate~~time-scale, κ is a vertical diffusion and $S(\theta)$ account for the ~~convective sources~~distribution of high clouds.

The profile of the heating rate in the lower panel of Fig. 4 suggests that we can separate a region near the all sky LZRH θ_0 where the heating rate grows linearly with θ and another region above where the heating rate is essentially constant. In addition, as the LZRH lies above the level of maximum high cloud ~~, the source~~ cover, the high clouds can be represented by an exponential distribution $S(\theta) = S_0 \exp(-\beta(\theta-\theta_0))$ with the slope found in Fig. 4.

In the simplest version, we assume that ~~$\alpha = 0$~~ $\alpha^{-1} = 0$, therefore considering the global domain, and that the heating is $\dot{\theta} = \Lambda(\theta - \theta_0)$. In this case, (1) is a Fokker-Planck equation and it can be shown (Gardiner, 2009) that the probability of transit from θ_a to ~~θ_b~~ $\theta_b > \theta_a$ is

$$\Pi(\theta_a,\theta_b)=\frac{1+\mathrm{erf}\left(\nu(\theta_a-\theta_0)\right)}{1+\mathrm{erf}\left(\nu(\theta_b-\theta_0)\right)} \tag{2}$$

where $\nu = (2\kappa)^{-1/2}\Lambda^{1/2}$. Consequently, the distribution of convective sources that impact a given level is

$$P(\theta) = N^{-1} e^{-\beta(\theta-\theta_0)} \left(1 + \mathrm{erf}\left(\nu(\theta-\theta_0)\right)\right) \tag{3}$$

where ~~N is a constant . This distribution is plotted in~~ the dependency on the impact level is in the constant N. The upper panel of Fig.13 ~~and shows that ,~~ shows that according to the value of the ratio β/ν, the distribution of sources for parcels that travel to the target level θ is centred on the LZRH, below it or above it. Table 1 shows that over Land and Ocean, the proportion of sources above the LZRH is always large, up to 96% over the Ocean. Therefore we are in the case where $\beta > \nu$ and diffusion across the LZRH is negligible. The Tibetan ~~plateau~~ Plateau differs by exhibiting a majority of sources below the LZRH, especially for the ERA-Interim. This is consistent with the behaviour of the crossover and indicates that parcels rapidly travel outside the Tibetan ~~plateau~~Plateau, where the LZRH is lower, and they find ascending motion. On the overall, this suggests that the LZRH is an effective barrier and that diffusion due to fluctuating heating rates and explicit gravity waves resolved by the ~~reanalysis do not allow to cross it~~reanalyses is not large enough to overcome the barrier.

In the second stage, we neglect diffusion and we assume that $\dot{\theta} = \Lambda(\theta - \theta_0)$ from θ_0 to θ_1, above which the heating rate is assumed to be constant equal to $A = \Lambda(\theta_1 - \theta_0)$. The LZRH is then a perfect barrier and we consider only the cloud sources above θ_0 described with the same exponential distribution as in the previous stage. This problem can be fully solved (see Sect. S9 of the Supplement) and ~~Figure ?? shows how the solution varies~~ the solution is illustrated in the lower panel of Fig. 13, as a function of ~~the parameter~~age at the level $\theta = 380$ K, for the basic set of parameters $\theta_0 = 360$ K, $\theta_1 = 370$ K, $\Lambda = 0.1$ day^{-1}, $\beta = 0.4$ K^{-1}, $\alpha = 10$ day and $A = 1$ K day^{-1}, that mimic the situation for the ERA5 diabatic transport in the monsoon area. The modal age and mean age are about 30 days in rough agreement with Figs. S5 and S6 of the Supplement. Figure 13 also shows the effect of changing the parameters by multiplying Λ by 3, β by 0.4, α by 0.5 and A by 3. It is visible that, for the displayed regime, Λ basically controls the width of the distribution without changing the modal age. Changing α both changes the shape and the modal age. The parameter β, when reduced, leads to a new regime where the maximum is attained at $t = (\theta - \theta_1)/A$. When increased or less decreased (not shown), the effect is mainly a translation in time. A performs essentially a translation in time. A full interactive solution as a function of the parameters is available in the Supplementary material as a Computable Document Format notebook playable with Wolfram Player (https://www.wolfram.com/player/)~~as Supplementary material~~.

In the third stage, we calculate the solution by using the ERA5 and ERA-Interim heating ~~within the AMACore region~~ rates within the restricted domain (20°E-140°E and 10°N-40°N) already used in Fig. 4 and the vertical distribution of the cloud sources used in the 3D calculations as shown in Fig. 4. The erosion time-scale α is fixed at 13.3 day and $\kappa = 0.1$ K^{2}day^{-1} (that is about 0.05 m^{2}s^{-1}) is used to regularize the solution. Figure 14 shows the distribution of impact as a function of age and potential temperature to be compared with the right column of Fig. 5. ~~Here $\kappa = 0.1$ m^{2}s^{-1} has been used to regularize the solution.~~ The 1D model reproduces very well the main character of ascent and descent, albeit the temporal decay is faster than in the 3D calculations. A more quantitative comparison is made in Fig. 15 for ERA5 and the ~~same~~ three isentropic levels ~~as Fig. ??~~370 K, 380 K and 390 K, for several values of κ. We see that the diffusion basically slows the upward propagation but does not change qualitatively the solution. ~~The~~ In view of its simplicity, the 1D model ~~shows results close enough to~~ is very

successful at reproducing the 3D solution, ~~providing a bulk~~ which means that it provides a relevant explanation of the mean transport and confinement properties of the AMA.

5 Conclusions

We have studied the transport pathways from injection at the top of the high convective clouds to the lower tropical stratosphere during the Asian monsoon, using ~~massive~~ a very dense set of Lagrangian trajectories driven by observed clouds and reanalysis data. ~~It has been shown~~ We show that, unlike ~~in~~ the ERA-Interim, kinematic and diabatic trajectories of the ERA5 provide a consistent description of the motion above the LZRH. The kinematic and diabatic trajectories differ below the LZRH (missing in the kinematic case) within the convective region. However, both methods capture the descending motion over the deserts and the descending branches of the Hadley-Walker circulation.

~~There is a dichotomy among convective parcels which are injected above or below~~ The path of convective parcels depends on whether they are injected below or above the crossover level. Below this level they are mostly entrained horizontally within the Hadley-Walker circulation towards regions of subsidence, where they return to lower levels. Above the crossover, parcels are entrained into the upward motion that lead them to cross the tropopause and enter the stratosphere. The crossover is at 364.4 K over Asia land with no significant difference over the Tibetan Plateau and is 2 K lower over the ocean. Only a small part of the convective clouds (2.6% on the average) ~~reaches~~ reach high enough, above the crossover, to inject parcels that move further upward. Due to the exponential decay of convective top frequency with altitude, the crossover is usually located above the LZRH, which appears as an effective barrier to vertical transport. The Tibetan ~~plateau~~ Plateau is an exception with a crossover lower than the LZRH~~but still close to that of surrounding land.~~. This can be explained by the relatively small size of the plateau relative to the AMA and the ease of parcels to leave it by horizontal motion and subsequently find ascent motion in nearby regions of Asia.

In the region above ~~360~~ the crossover, the confinement within the AMA is the result of the constant renewal by fresh convective inflow and the leaky circulation of the AMA. As a result, the younger air is found at the core of the anticyclone and the oldest air is found at its periphery where it is expelled with a time-scale of about 13 days~~. This time is~~ , which is of the same order but shorter than the returning time of the mean circulation (about 2 to 3 weeks). ~~As the level rises, the confined Asian monsoon air is more and more diluted and replaced by older air which comes from other regions~~The erosion combines with a mean ascent rate of 1.1 $\mathrm{K day}^{-1}$ to generate an exponential dilution with altitude. The dilution, partly due to the volume expansion, is compatible with the persistence of a strong convective influence within the AMA, through the whole TTL as background air is mostly kept outside, thereby causing the appearance of a columnar tracer pattern found in many observations and modelling studies (Park et al., 2009; Randel et al., 2010; Pan et al., 2016). This process is akin to the "blower" hypothesis of Pan et al. (2016) except that it is uniformly distributed over the whole range of altitude from the crossover to 420 K at least. The ascent occurs therefore following a broad spiral, as advocated by Vogel et al. (2019).

The air that is trapped within the AMA comes mainly from continental convection. The sources exhibit a concentration in North India and the south of the Tibetan Plateau, as found in many previous studies ~~(e.g., Bergman et al., 2015; Tissier and Legras, 2016)~~(e.

We find that, for continental convection as a whole, this result is partly due to the higher level of convection over land than over ocean. The localization of the convective sources and of the associated convective towers carrying air from the boundary layer was identified as a vertical "conduit" by Bergman et al. (2013). However, this conduit ends exactly at the level of cloud detrainment.

The Tibetan ~~plateau~~ Plateau is favoured by its location at the core of the AMA and is also the region that exhibits the largest amount of high clouds above the crossover. This suggests that the compounds released at the ground there have the highest chance to reach the stratosphere. However, we find that the impact of the Tibetan ~~plateau~~ Plateau at 380 K is entirely explained by the high proportion of clouds above the crossover. There is no indication of a favoured ascent above the Tibetan clouds. On the contrary, the fact that the crossover is lower than the local LZRH indicates that parcels leave the Tibetan ~~plateau~~ Plateau to perform the ascent over other regions inside the AMA.

We find that the ~~bulk~~ mean properties of upward transport and confinement within the AMA over the whole summer can be explained by a simple 1D ~~model,~~ diffusive-advective-loss model, with a constant loss rate, forced by the observed distribution of convective sources and heating rates~~and with a constant loss rate. The~~ . A main ingredient to get an impact with both a maximum in age and altitude ~~sections~~ is that, between 360 K and 370 K, the heating grows from the LZRH and that it stays roughly constant above 370 K up to the lower stratosphere. This is entirely consistent with the ~~other findings and the ascent within the AMAas a broad spiral, as advocated by Vogel et al. (2019), rather than concentrated in a narrow pipe~~demonstrated broad and regular ascent in the AMA.

Our diagnostics are based on whole summer averages and ignore the variability during the season. Section S10 of the Supplement ~~touches that question and show~~ deals with this issue and shows that, at least in 2017, the pattern of the impact confinement does not change significantly over the whole summer, in spite of noticeable modulations in amplitudes and distribution within the AMA. The fact that the characteristic loss time is smaller than the circulation time indicates that the AMA confinement is fragile. It is modulated both by the source convective activity underneath, which is subject to a number of oscillations of the Monsoon, and by the modulation of filament shredding on the west and east edges which is also irregular, as discussed, e.g., in Pan et al. (2016) and Vogel et al. (2015). The coupling between these processes has been recently considered by Ortega et al. (2017) and Wei et al. (2019).

The forward trajectories ignore possible intersections with clouds after launch. ~~It has been shown by Tissier and Legras (2016)~~ Tissier and that accounting such effect has a very small ~~effect~~ impact on the statistics of upward motion which is here our main focus.

Our study is also limited by the quality of the observations and of the ~~reanalysis~~reanalyses. The estimation of high clouds from geostationary infra-red imagers is subject to a number of uncertainties, in particular due to the cover of semi-transparent cirrus clouds above the anvils. The SAF-NWC algorithm detects such features but there are discontinuities in cloud classification between MSG1 and Himawari-8 which have also a visible impact on the cloud height estimation. Combining imagers with sounders which are highly sensitive to ice clouds (Stubenrauch et al., 2013) will provide in the future a way to improve ~~this~~ these retrievals.

~~The~~ Several recent studies (Hoffmann et al., 2019; Tegtmeier et al., 2020; Bucci et al., 2019) showed that the ERA5 ~~was shown in several recent studies (Hoffmann et al., 2019; **?**; Bucci et al., 2019) to provide a better~~ improves the representation

of atmospheric properties, including transport. The ERA5 is, however, singular in favouring very high penetrative convection over the Tibetan ~~plateau~~ Plateau which should be considered with caution due to the lack of data and of training of the model over this region.

~~The Tibetan plateau~~The Tibetan Plateau, in spite of its limited global impact, is a region of high interest to understand transport within the AMA. The lack of high quality observations with active instruments, both from the ground and from space (as current active instruments do not overpass the region in the evening when convection is the most active) hampers our understanding of convection over this region and certainly deserves some efforts to bridge the gap.

More generally, the fact that the clouds that contribute to the upward flux in the TTL and in the stratosphere are a small fraction within the upper tail distribution opens the question of the role of small-scale intermittent overshooting convection above the anvils which is seldom observed by the geostationary satellites. Although the effect was found by James et al. (2008) to be small in the Asian Monsoon region, this deserves further investigation within the context of Lagrangian studies.

On the overall, our estimates of the convective impact using high resolution datasets and advanced satellite products essentially corroborate that of Tissier and Legras (2016), made with lower resolution data and less advanced estimates of the high clouds. It is also in good qualitative agreement with Garny and Randel (2016) regarding the role of the crossover and with Orbe et al. (2015) and Vogel et al. (2019) regarding the distribution of sources and provide new interpretation to the works of Bergman et al. (2013) and Pan et al. (2016).

Code and data availability. Most of the programs used in this study are freely available and documented under github bernard-legras. This study generated a multi-terabyte ensemble of trajectories and post-processed files stored on the Institut Pierre-Simon Laplace meso-centre. They are all available from the main author upon request.

Author contributions. The design of the experiments, Lagrangian calculations and data processing have been performed by B.L. The analysis and the writing of the manuscript have been performed by B.L and S.B.

Competing interests. The authors declare no conflict of interest

Acknowledgements. We thank Alexandra Tzella for pointing out the Gardiner's solution to the exit time problem. This work was supported by the StratoClim project by the European Community Seventh Framework Programme (FP7/2007–2013) under grant agreement no. 603557, and by the CEFIPRA 5607-1 and the TTL-Xing ANR-17-CE01-0015 projects. ~~We thank the whole StratoClim Team for having made this successful campaign possible.~~ Meteorological analysis data ~~are~~ were provided by the European Centre for Medium-Range Weather Forecasts. ERA-5 trajectory computations ~~are~~ were generated using Copernicus Climate Change Service Information. We also thank the AERIS Data

and Service Centre for providing access to the MSG1 and Himawari data and ~~processing tools.~~ to processing resources The Eumetsat SAF-NWC, and in particular Hervé le Gléau and Gaëlle Kerdraon, are thanked for giving access to their software

References

Bergman, J. W., Jensen, E. J., Pfister, L., and Yang, Q.: Seasonal Differences of Vertical-Transport Efficiency in the Tropical Tropopause Layer: On the Interplay between Tropical Deep Convection, Large-Scale Vertical Ascent, and Horizontal Circulations, Journal of Geophysical Research, 117, D05 302, https://doi.org/10.1029/2011JD016992, 2012.

Bergman, J. W., Fierli, F., Jensen, E. J., Honomichl, S., and Pan, L. L.: Boundary Layer Sources for the Asian Anticyclone: Regional Contributions to a Vertical Conduit, Journal of Geophysical Research: Atmospheres, 118, 2560–2575, https://doi.org/10.1002/jgrd.50142, 2013.

Bergman, J. W., Pfister, L., and Yang, Q.: Identifying Robust Transport Features of the Upper Tropical Troposphere, Journal of Geophysical Research: Atmospheres, 120, 6758–6776, https://doi.org/10.1002/2015JD023523, 2015.

Berry, E. and Mace, G. G.: Cloud Properties and Radiative Effects of the Asian Summer Monsoon Derived from A-Train Data, Journal of Geophysical Research: Atmospheres, 119, 9492–9508, https://doi.org/10.1002/2014JD021458, 2014.

Bucci, S., Legras, B., Sellitto, P., D'Amato, F., Viciani, S., Montori, A., Chiarugi, A., Ravegnani, F., Ulanovsky, A., Cairo, F., and Stroh, F.: Deep Convective Influence on the UTLS Composition in the Asian Monsoon Anticyclone Region: 2017 StratoClim Campaign Results, Atmospheric Chemistry and Physics Discussions, https://doi.org/10.5194/acp-2019-1053, 2019.

Copernicus Climate Change Service (C3S): ERA5: Fifth Generation of ECMWF Atmospheric Reanalyses of the Global Climate, Tech. rep., Copernicus Climate Change Service Climate Data Store (CDS), 2017.

Corti, T., Luo, B. P., Fu, Q., Vömel, H., and Peter, T.: The Impact of Cirrus Clouds on Tropical Troposphere-to-Stratosphere Transport, Atmospheric Chemistry and Physics, 6, 2539–2547, https://doi.org/10.5194/acp-6-2539-2006, 2006.

Dee, D. P., Uppala, S. M., Simmons, A. J., Berrisford, P., Poli, P., Kobayashi, S., Andrae, U., Balmaseda, M. A., Balsamo, G., Bauer, P., Bechtold, P., Beljaars, A. C. M., Van de Berg, L. V. D., Bidlot, J., Bormann, N., Delsol, C., Dragani, R., Fuentes, M., Geer, A. J., Haimberger, L., Healy, S. B., Hersbach, H., Hólm, E. V., Isaksen, L., Kå llberg, P., Köhler, M., Matricardi, M., McNally, A. P., Monge-Sanz, B. M., Morcrette, J. J., Park, B.-K., Peubey, C., de Rosnay, P., Tavolato, C., Thépaut, J.-N., and Vitart, F.: The ERA-Interim Reanalysis : Configuration and Performance of the Data Assimilation System, Quarterly Journal of the Royal Meteorological Society, 137, 553–597, https://doi.org/10.1002/qj.828, 2011.

Derrien, M. and Le Gléau, H.: Improvement of Cloud Detection near Sunrise and Sunset by Temporal-Differencing and Region-Growing Techniques with Real-Time SEVIRI, International Journal of Remote Sensing, 31, 1765–1780, https://doi.org/10.1080/01431160902926632, 2010.

Fan, Q., Bian, J., and Pan, L. L.: Stratospheric Entry Point for Upper-Tropospheric Air within the Asian Summer Monsoon Anticyclone, Science China Earth Sciences, 60, 1685–1693, https://doi.org/10.1007/s11430-016-9073-5, 2017.

Fueglistaler, S., Dessler, A. E., Dunkerton, T. J., Folkins, I., Fu, Q., and Mote, P. W.: Tropical Tropopause Layer, Reviews of Geophysics, 47, RG1004, https://doi.org/10.1029/2008RG000267, 2009.

Gardiner, C. W.: Stochastic Methods: A Handbook for the Natural and Social Sciences, Springer Series in Synergetics, Springer, Berlin, 4th ed edn., 2009.

Garny, H. and Randel, W. J.: Dynamic Variability of the Asian Monsoon Anticyclone Observed in Potential Vorticity and Correlations with Tracer Distributions, Journal of Geophysical Research: Atmospheres, 118, 13,421–13,433, https://doi.org/10.1002/2013JD020908, 2013.

Garny, H. and Randel, W. J.: Transport Pathways from the Asian Monsoon Anticyclone to the Stratosphere, Atmospheric Chemistry and Physics, 16, 2703–2718, https://doi.org/10.5194/acp-16-2703-2016, 2016.

Hartmann, D. L. and Larson, K.: An Important Constraint on Tropical Cloud - Climate Feedback, Geophysical Research Letters, 29, 1951–1951, https://doi.org/10.1029/2002GL015835, 2002.

Hersbach, H., Bell, W., Berrisford, P., Horányi, A., J., M.-S., Nicolas, J., Radu, R., Schepers, D., Simmons, A., Soci, C., and Dee, D.: Global Reanalysis: Goodbye ERA-Interim, Hello ERA5, ECMWF Newsletter, 159, 17–24, https://doi.org/10.21957/VF291HEHD7, 2019.

Hoffmann, L., Günther, G., Li, D., Stein, O., Wu, X., Griessbach, S., Heng, Y., Konopka, P., Müller, R., Vogel, B., and Wright, J. S.: From ERA-Interim to ERA5: The Considerable Impact of ECMWF's next-Generation Reanalysis on Lagrangian Transport Simulations, Atmospheric Chemistry and Physics, 19, 3097–3124, https://doi.org/10.5194/acp-19-3097-2019, 2019.

James, R., Bonazzola, M., Legras, B., Surbled, K., and Fueglistaler, S.: Water Vapor Transport and Dehydration above Convective Outflow during Asian Monsoon, Geophysical Research Letters, 35, L20 810, https://doi.org/10.1029/2008GL035441, 2008.

Johansson, E., Devasthale, A., L'Ecuyer, T., Ekman, A. M. L., and Tjernström, M.: The Vertical Structure of Cloud Radiative Heating over the Indian Subcontinent during Summer Monsoon, Atmospheric Chemistry and Physics, 15, 11 557–11 570, https://doi.org/10.5194/acp-15-11557-2015, 2015.

Joseph, B. and Legras, B.: Relation between Kinematic Boundaries, Stirring, and Barriers for the Antarctic Polar Vortex, Journal of the Atmospheric Sciences, 59, 1198–1212, https://doi.org/10.1175/1520-0469(2002)059<1198:RBKBSA>2.0.CO;2, 2002.

Li, D., Vogel, B., Müller, R., Bian, J., Günther, G., Plöger, F., Li, Q., Zhang, J., Bai, Z., Vömel, H., and Riese, M.: Dehydration and Low Ozone in the Tropopause Layer over the Asian Monsoon Caused by Tropical Cyclones: Lagrangian Transport Calculations Using ERA-Interim and ERA5 Reanalysis Data, Preprint, Dynamics/Atmospheric Modelling/Troposphere/Physics (physical properties and processes), https://doi.org/10.5194/acp-2019-816, 2019.

Luo, J., Pan, L. L., Honomichl, S. B., Bergman, J. W., Randel, W. J., Francis, G., Clerbaux, C., George, M., Liu, X., and Tian, W.: Space–Time Variability in UTLS Chemical Distribution in the Asian Summer Monsoon Viewed by Limb and Nadir Satellite Sensors, Atmospheric Chemistry and Physics, 18, 12 511–12 530, https://doi.org/10.5194/acp-18-12511-2018, 2018.

McFarlane, S. A., Mather, J. H., and Ackerman, T. P.: Analysis of Tropical Radiative Heating Profiles: A Comparison of Models and Observations, Journal of Geophysical Research, 112, D14 218, https://doi.org/10.1029/2006JD008290, 2007.

Orbe, C., Waugh, D. W., and Newman, P. A.: Air-Mass Origin in the Tropical Lower Stratosphere: The Influence of Asian Boundary Layer Air, Geophysical Research Letters, 42, 4240–4248, https://doi.org/10.1002/2015GL063937, 2015.

Ortega, S., Webster, P. J., Toma, V., and Chang, H.-R.: Quasi-Biweekly Oscillations of the South Asian Monsoon and Its Co-Evolution in the Upper and Lower Troposphere, Climate Dynamics, 49, 3159–3174, https://doi.org/10.1007/s00382-016-3503-y, 2017.

Pan, L. L., Honomichl, S. B., Kinnison, D. E., Abalos, M., Randel, W. J., Bergman, J. W., and Bian, J.: Transport of Chemical Tracers from the Boundary Layer to Stratosphere Associated with the Dynamics of the Asian Summer Monsoon, Journal of Geophysical Research: Atmospheres, 121, 14,159–14,174, https://doi.org/10.1002/2016JD025616, 2016.

Park, M., Randel, W. J., Gettelman, A., Massie, S. T., and Jiang, J. H.: Transport above the Asian Summer Monsoon Anticyclone Inferred from Aura Microwave Limb Sounder Tracers, Journal of Geophysical Research, 112, D16 309–D16 309, https://doi.org/10.1029/2006JD008294, 2007.

Park, M., Randel, W. J., Emmons, L. K., Bernath, P. F., Walker, K. A., and Boone, C. D.: Chemical Isolation in the Asian Monsoon Anticyclone Observed in Atmospheric Chemistry Experiment (ACE-FTS) Data, Atmospheric Chemistry and Physics, 8, 757–764, https://doi.org/10.5194/acp-8-757-2008, 2008.

Park, M., Randel, W. J., Emmons, L. K., and Livesey, N. J.: Transport Pathways of Carbon Monoxide in the Asian Summer Monsoon Diagnosed from Model of Ozone and Related Tracers (MOZART), Journal of Geophysical Research, 114, D08 303–D08 303, https://doi.org/10.1029/2008JD010621, 2009.

Pisso, I. and Legras, B.: Turbulent Vertical Diffusivity in the Sub-Tropical Stratosphere, Atmospheric Chemistry and Physics, 8, 697–707, https://doi.org/10.5194/acp-8-697-2008, 2008.

Ploeger, F., Konopka, P., Müller, R., Fueglistaler, S., Schmidt, T., Manners, J. C., Grooß, J.-U., Günther, G., Forster, P. M., and Riese, M.: Horizontal Transport Affecting Trace Gas Seasonality in the Tropical Tropopause Layer (TTL), Journal of Geophysical Research, 117, D09 303, https://doi.org/10.1029/2011JD017267, 2012.

Ploeger, F., Gottschling, C., Griessbach, S., Grooß, J.-U., Guenther, G., Konopka, P., Müller, R., Riese, M., Stroh, F., Tao, M., Ungermann, J., Vogel, B., and von Hobe, M.: A Potential Vorticity-Based Determination of the Transport Barrier in the Asian Summer Monsoon Anticyclone, Atmospheric Chemistry and Physics, 15, 13 145–13 159, https://doi.org/10.5194/acp-15-13145-2015, 2015.

Ploeger, F., Konopka, P., Walker, K., and Riese, M.: Quantifying Pollution Transport from the Asian Monsoon Anticyclone into the Lower Stratosphere, Atmospheric Chemistry and Physics, 17, 7055–7066, https://doi.org/10.5194/acp-17-7055-2017, 2017.

Randel, W. J. and Jensen, E. J.: Physical Processes in the Tropical Tropopause Layer and Their Roles in a Changing Climate, Nature Geoscience, 6, 169–176, https://doi.org/10.1038/ngeo1733, 2013.

Randel, W. J. and Park, M.: Deep Convective Influence on the Asian Summer Monsoon Anticyclone and Associated Tracer Variability Observed with Atmospheric Infrared Sounder (AIRS), Journal of Geophysical Research, 111, D12 314–D12 314, https://doi.org/10.1029/2005JD006490, 2006.

Randel, W. J., Park, M., Wu, F., and Livesey, N.: A Large Annual Cycle in Ozone above the Tropical Tropopause Linked to the Brewer–Dobson Circulation, Journal of the Atmospheric Sciences, 64, 4479–4488, https://doi.org/10.1175/2007JAS2409.1, 2007.

Randel, W. J., Park, M., Emmons, L., Kinnison, D., Bernath, P., a Walker, K., Boone, C., and Pumphrey, H.: Asian Monsoon Transport of Pollution to the Stratosphere., Science, 328, 611–613, https://doi.org/10.1126/science.1182274, 2010.

Santee, M. L., Manney, G. L., Livesey, N. J., Schwartz, M. J., Neu, J. L., and Read, W. G.: A Comprehensive Overview of the Climatological Composition of the Asian Summer Monsoon Anticyclone Based on 10 Years of Aura Microwave Limb Sounder Measurements, Journal of Geophysical Research: Atmospheres, 122, 5491–5514, https://doi.org/10.1002/2016JD026408, 2017.

Sèze, G., Pelon, J., Derrien, M., Le Gléau, H., and Six, B.: Evaluation against CALIPSO Lidar Observations of the Multi-Geostationary Cloud Cover and Type Dataset Assembled in the Framework of the Megha-Tropiques Mission: Evaluation of a Multi-Geostationary Cloud Cover Set Using CALIOP Data, Quarterly Journal of the Royal Meteorological Society, 141, 774–797, https://doi.org/10.1002/qj.2392, 2015.

Stohl, A., Forster, C., Frank, A., Seibert, P., and Wotawa, G.: Technical Note: The Lagrangian Particle Dispersion Model FLEXPART Version 6.2, Atmospheric Chemistry and Physics, 5, 2461–2474, https://doi.org/10.5194/acp-5-2461-2005, 2005.

Stubenrauch, C. J., Rossow, W. B., Kinne, S., Ackerman, S., Cesana, G., Chepfer, H., Di Girolamo, L., Getzewich, B., Guignard, A., Heidinger, A., Maddux, B. C., Menzel, W. P., Minnis, P., Pearl, C., Platnick, S., Poulsen, C., Riedi, J., Sun-Mack, S., Walther, A., Winker, D., Zeng, S., and Zhao, G.: Assessment of Global Cloud Datasets from Satellites: Project and Database Initiated by the GEWEX Radiation Panel, Bulletin of the American Meteorological Society, 94, 1031–1049, https://doi.org/10.1175/BAMS-D-12-00117.1, 2013.

Tegtmeier, S., Krüger, K., Birner, T., Davis, N. A., Davis, S., Fujiwara, M., Homeyer, C. R., Ivanciu, I., Kim, Y.-H., Legras, B., Manney, G. L., Nishimoto, E., Nützel, M., Kedzierski, R. P., Wang, J. S., Wang, T., and Wright, J. S.: Tropical Tropopause Layer, Stratosphere-Troposphere Processes And Their Role in Climate, Chapter 8, Submitted, (SPARC) Reanalysis Intercomparison Project (S-RIP) Report, 2019.

Tegtmeier, S., Anstey, J., Davis, S., Dragani, R., Harada, Y., Ivanciu, I., Pilch Kedzierski, R., Krüger, K., Legras, B., Long, C., Wang, J. S., Wargan, K., and Wright, J. S.: Temperature and Tropopause Characteristics from Reanalyses Data in the Tropical Tropopause Layer, Atmospheric Chemistry and Physics, 20, 753–770, https://doi.org/10.5194/acp-20-753-2020, 2020.

Tissier, A.-S. and Legras, B.: Convective Sources of Trajectories Traversing the Tropical Tropopause Layer, Atmospheric Chemistry and Physics, 16, 3383–3398, https://doi.org/10.5194/acp-16-3383-2016, 2016.

Tzella, A. and Legras, B.: A Lagrangian View of Convective Sources for Transport of Air across the Tropical Tropopause Layer: Distribution, Times and the Radiative Influence of Clouds, Atmospheric Chemistry and Physics, 11, 12 517–12 534, https://doi.org/10.5194/acp-11-12517-2011, 2011.

Vernier, J.-P., Fairlie, T. D., Natarajan, M., Wienhold, F. G., Bian, J., Martinsson, B. G., Crumeyrolle, S., Thomason, L. W., and Bedka, K. M.: Increase in Upper Tropospheric and Lower Stratospheric Aerosol Levels and Its Potential Connection with Asian Pollution: ATAL Nature and Origin, Journal of Geophysical Research: Atmospheres, 120, 1608–1619, https://doi.org/10.1002/2014JD022372, 2015.

Vogel, B., Günther, G., Müller, R., Grooß, J.-U., and Riese, M.: Impact of Different Asian Source Regions on the Composition of the Asian Monsoon Anticyclone and of the Extratropical Lowermost Stratosphere, Atmospheric Chemistry and Physics, 15, 13 699–13 716, https://doi.org/10.5194/acp-15-13699-2015, 2015.

Vogel, B., Müller, R., Günther, G., Spang, R., Hanumanthu, S., Li, D., Riese, M., and Stiller, G. P.: Lagrangian Simulations of the Transport of Young Air Masses to the Top of the Asian Monsoon Anticyclone and into the Tropical Pipe, Atmospheric Chemistry and Physics, 19, 6007–6034, https://doi.org/10.5194/acp-19-6007-2019, 2019.

Wei, W., Zhang, R., Yang, S., Li, W., and Wen, M.: Quasi-Biweekly Oscillation of the South Asian High and Its Role in Connecting the Indian and East Asian Summer Rainfalls, Geophysical Research Letters, p. 2019GL086180, https://doi.org/10.1029/2019GL086180, 2019.

Wright, J. S. and Fueglistaler, S.: Large Differences in Reanalyses of Diabatic Heating in the Tropical Upper Troposphere and Lower Stratosphere, Atmospheric Chemistry and Physics, 13, 9565–9576, https://doi.org/10.5194/acp-13-9565-2013, 2013.

Wright, J. S., Fu, R., Fueglistaler, S., Liu, Y. S., and Zhang, Y.: The Influence of Summertime Convection over Southeast Asia on Water Vapor in the Tropical Stratosphere, Journal of Geophysical Research, 116, D12 302, https://doi.org/10.1029/2010JD015416, 2011.

Wu, Y., Orbe, C., Tilmes, S., Abalos, M., and Wang, X.: Fast Transport Pathways Into the Northern Hemisphere Upper Troposphere and Lower Stratosphere During Northern Summer, Journal of Geophysical Research: Atmospheres, 125, https://doi.org/10.1029/2019JD031552, 2020.

Yan, R. and Bian, J.: Tracing the Boundary Layer Sources of Carbon Monoxide in the Asian Summer Monsoon Anticyclone Using WRF-Chem, Advances in Atmospheric Sciences, 32, 943–951, https://doi.org/10.1007/s00376-014-4130-3, 2015.

Yang, Q., Fu, Q., and Hu, Y.: Radiative Impacts of Clouds in the Tropical Tropopause Layer, Journal of Geophysical Research, 115, D00H12, https://doi.org/10.1029/2009JD012393, 2010.

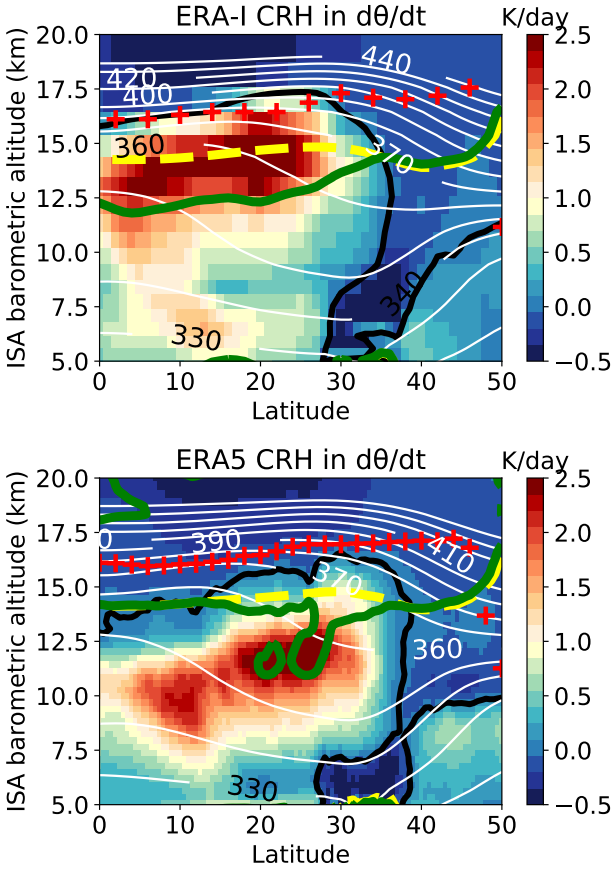

Figure 1. Cloud radiative heating (CRH) contribution to $d\theta/dt$ (in $\mathrm{K\,day^{-1}}$) averaged over July-August 2017 in the 73°E-97°E longitude range. Upper panel: ERA-Interim. Lower panel: ERA5. The black contour shows the zero line of CRH. White contours show potential temperature (in K). Red crosses show the cold point tropopause. The yellow line shows the level of zero clear sky radiative heating. The green contour shows the level of zero all sky radiative heating (LZRH). The small green contour by 20 km above the equator in the ERA5 is associated with a weak descent in this region. The vertical axis is the barometric altitude derived from pressure using the hydrostatic equation and the standard atmosphere. The true geopotential altitude is higher, up to +850 m on the 360 K surface near 30N (see Fig. S1 of the Supplement).

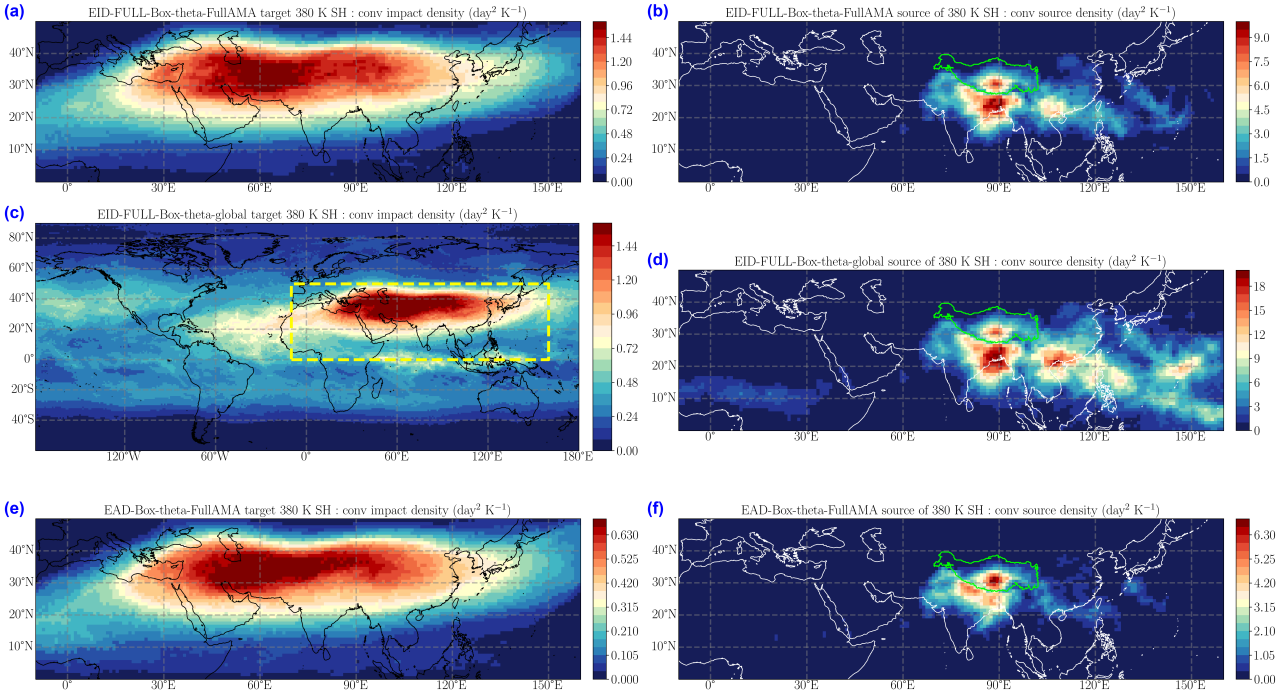

Figure 2. Impact density and source density for the convective parcels reaching the 380 K target level, accumulated over the ~~1~~ 1st June ~~2017 to~~ - 31 August 2017 launch interval and the two-month life time of the parcels. Left column (a,c,d): the impact density at the 380 K target level. Right column (b,c,e): the source density of convective clouds from which the parcels reaching 380 K have been launched. Upper row (a,b): ERA-Interim diabatic trajectories in the FullAMA domain. Mid-row (c,d): ERA-Interim diabatic trajectories in the global domain. Lower row (e,f): ERA5 diabatic trajectories in the FullAMA domain. The green contour on the right panels shows the Tibetan Plateau.

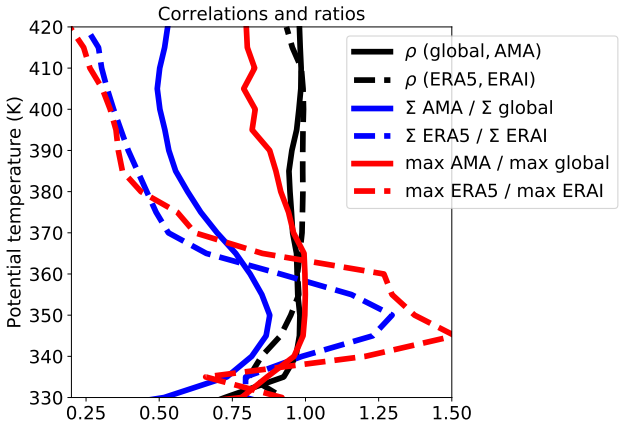

Figure 3. Solid back: correlation of the impact density between the FullAMA and global EID calculations within the FullAMA domain. Dash black: same for EAD and EID FullAMA calculations. Solid blue: ratio of maximum impacts between the FullAMA and global EID calculations within the FullAMA domain. Dash blue: same for EAD and EID FullAMA calculations. Solid red: ratio of cumulated impacts between the FullAMA and global EID calculations within the FullAMA domain. Dash ~~blue~~red: same for EAD and EID FullAMA calculations.

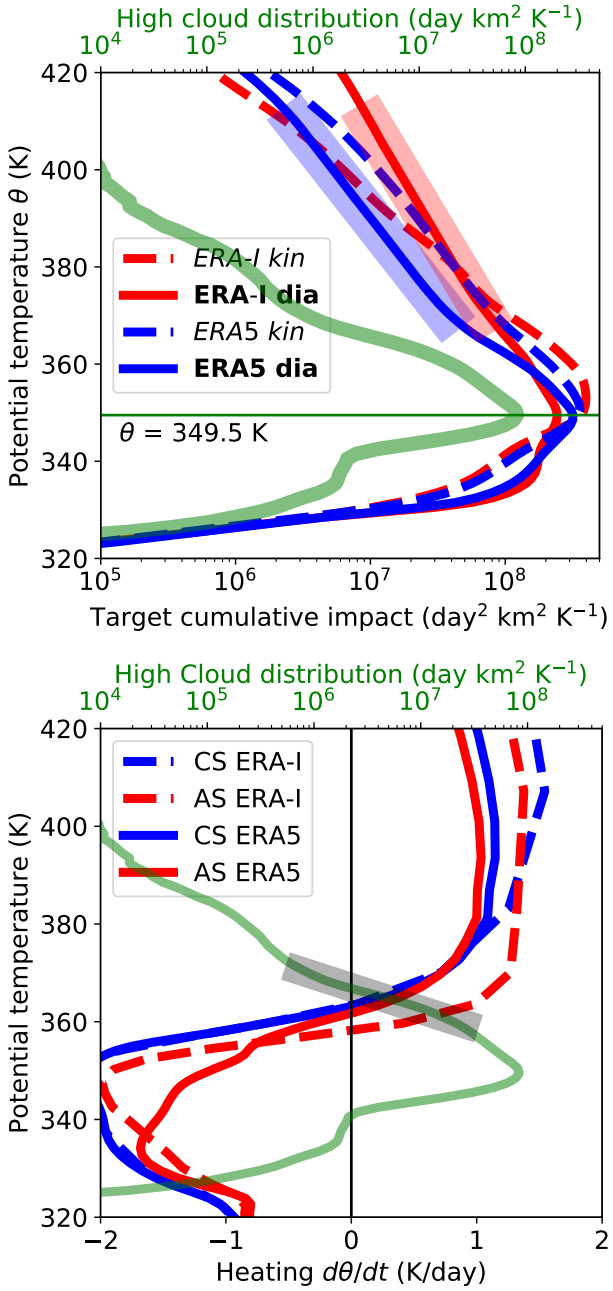

Figure 4. Upper panel. Green: Vertical distribution of the selected high cloud tops. Other curves: vertical distribution of the cumulated impact ~~integrated~~ within the FullAMA domain for the ~~EAD~~ ERA5 diabatic (EAD, solid blue), ~~EAZ~~ ERA5 kinematic (EAZ, dash blue), ~~EID~~ ERA-Interim diabatic (EID, solid red) and ~~EIZ~~ ERA-Interim kinematic (EIZ, dash red) experiments. For EAD and EID, a fit with a logarithmic decrement, respectively 0.065 K^{-1} and 0.050 K^{-1}, is shown between 370 K and 400 K (wide segments).

Lower panel. Green: same as in upper panel. Other curves: radiative heating rate profile average over the ~~CoreAMA~~ restricted domain (~~10~~20°~~E - 140~~E-140°E ~~,~~ and 10°~~N - 40~~N-40°N) ~~where the sources concentrate~~ for July and August 2017 ~~for~~ and all sky ERA5 (solid red), all sky ERA-Interim (dash red), clear sky ERA5 (solid blue) and clear sky ERA-Interim (dash blue). The fit of the high cloud distribution between 360 K and 370 K is shown with a logarithmic decrement $\beta = 0.325$ K^{-1} (wide segment).

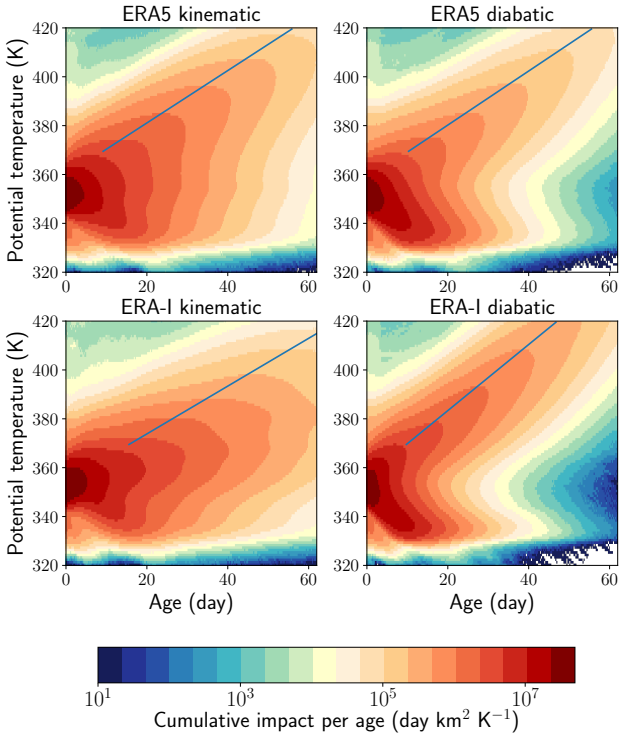

Figure 5. Distribution of the cumulated impact as a function of altitude and age with respect to the launch of the convective parcels. Upper row: ERA5. Lower row ERA-Interim. Left column: kinematic trajectories. Right column: diabatic trajectories. The slopes ~~are taken from~~ follow the crests of the distribution at each level (see also Sect. S4 of the Supplement).

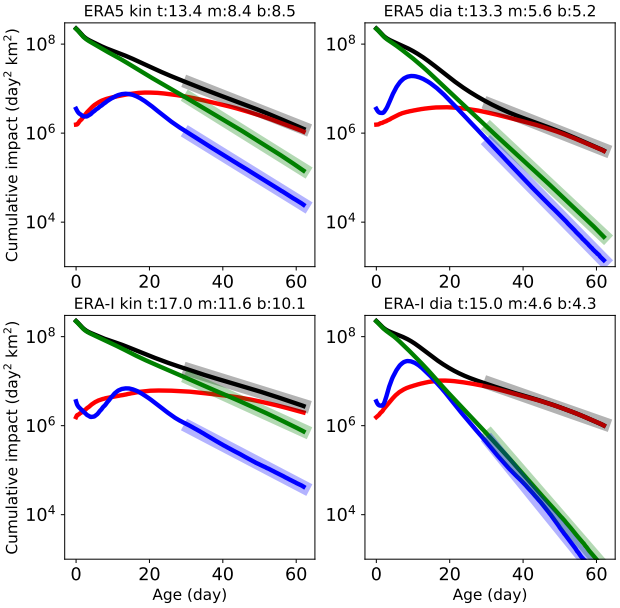

Figure 6. Evolution, as a function of age, of the total impact (black), the lower layer impact for $\theta < 340$ K (blue), the mid-layer impact for 340 K $< \theta <$ 370 K (green) and the upper layer impact for 370 K $< \theta$ (red). The four panels are arranged as in Fig. 5. The asymptotic e-folding time of the total and upper layer for the four cases are 13.4, 13.3, 17.0 and 15 day for, respectively, EAZ (ERA5-kin), EAD (ERA5-dia), EIZ (ERA-I kin) and EID (ERA-I dia). The asymptotic e-folding times (in days) for the top-layer (t), mid-layer (m) and bottom-layer (b) are listed in the title of each panel. They are calculated from the fit of an exponential law between ages 30 days and 62 days shown as wide segments in the figure.

~~Normalized distribution of the ages among convective parcels within the FullAMA domain at three isentropic levels 370 (blue), 380 (red) and 400 (black). The diamonds and the triangles show, respectively, the modal and the mean age for each curve. The four panels are arranged as in Fig. 5.~~

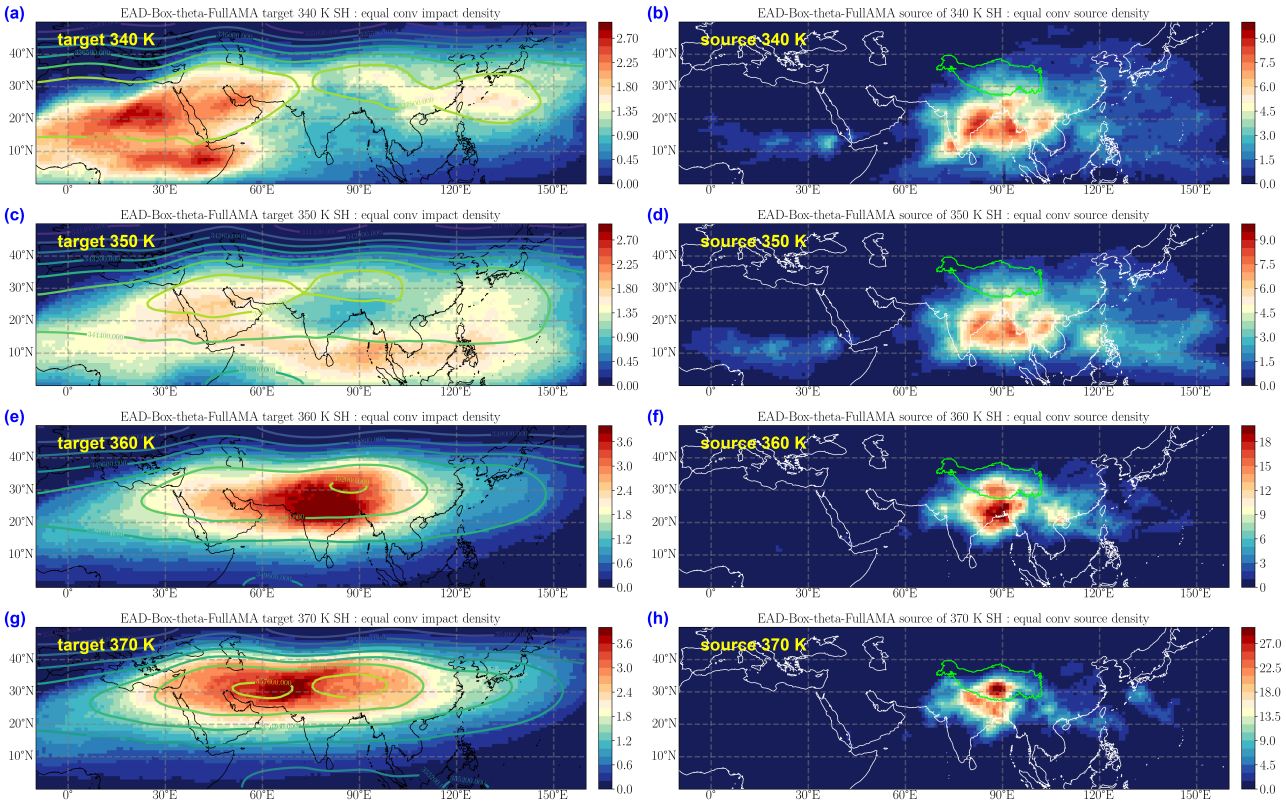

Figure 7. Left column (a,c,e,g): equalized impact density on isentropic levels (from top to bottom) (a) 340 K, (c) 350 K, (e) 360 K and (g) 370 K for ERA5 diabatic trajectories (EAD). Contours: Montgomery potential at the same levels. Right column (b,d,f,h): equalized source density for the same levels as in the left column and the same experiment. The green contour on the right panels shows the Tibetan Plateau.

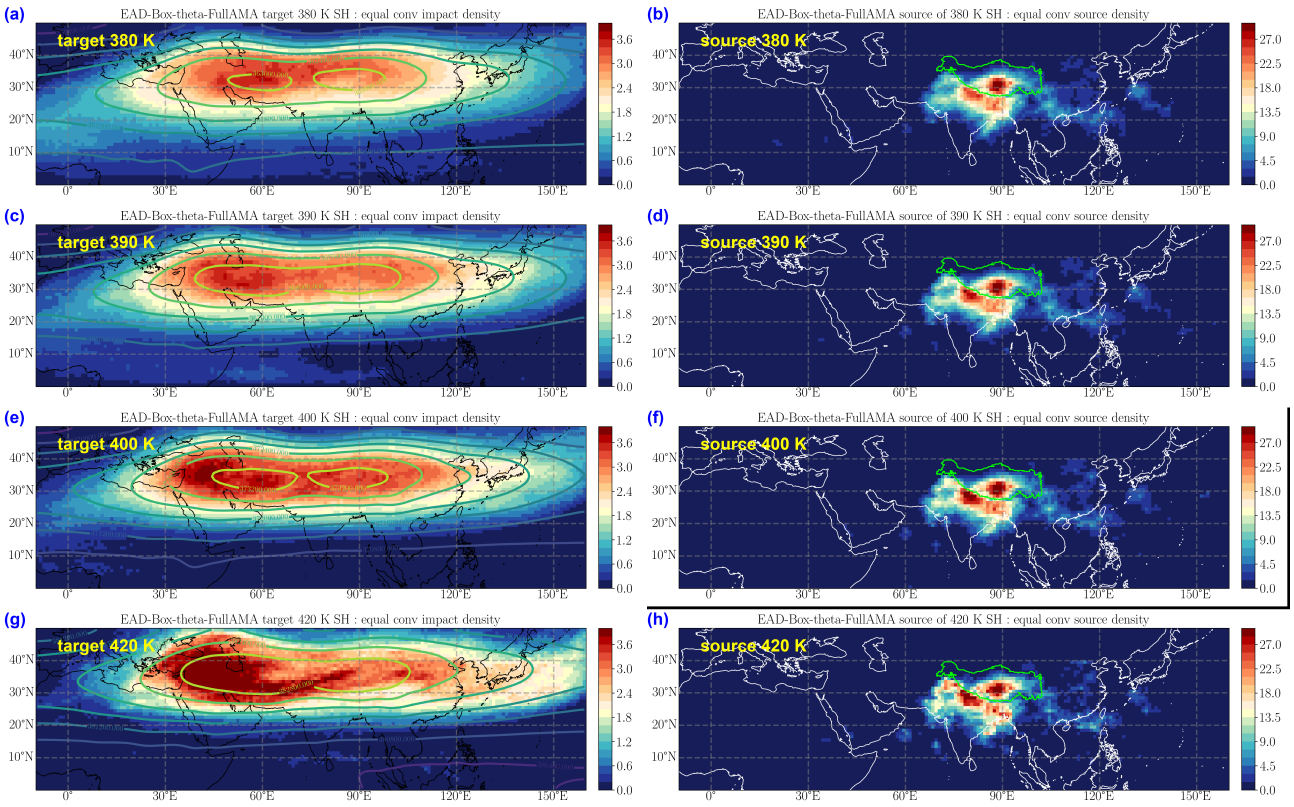

Figure 8. Same as Fig. 7 but for the levels (from top to bottom) 380 K, 390 K, 400 K and 420 K.

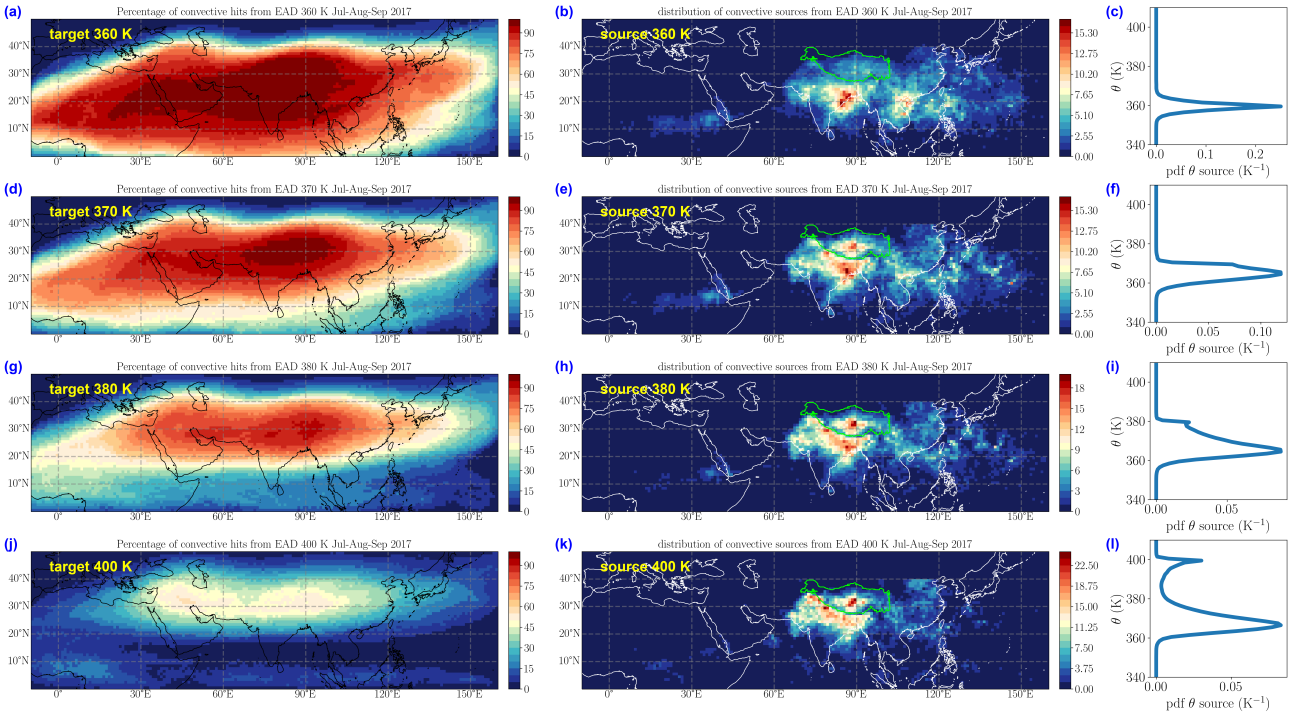

Figure 9. Left column (a,d,g,j): percentage of parcels hitting a convective cloud within 44 days ~~of~~ for ERA5 diabatic backward ~~trajectory~~ trajectories starting at 380 K (a), 390 K (b), 400 K (g) and 420 K (j) over the interval 1 July - 30 September 2017. ~~Center~~ Centre column (b,e,h,k): equalized source density for the same levels as in the left column and the same experiment. Right column: vertical probability density function (in K^{-1}) of the cumulated source density for the same levels as the two left other columns.

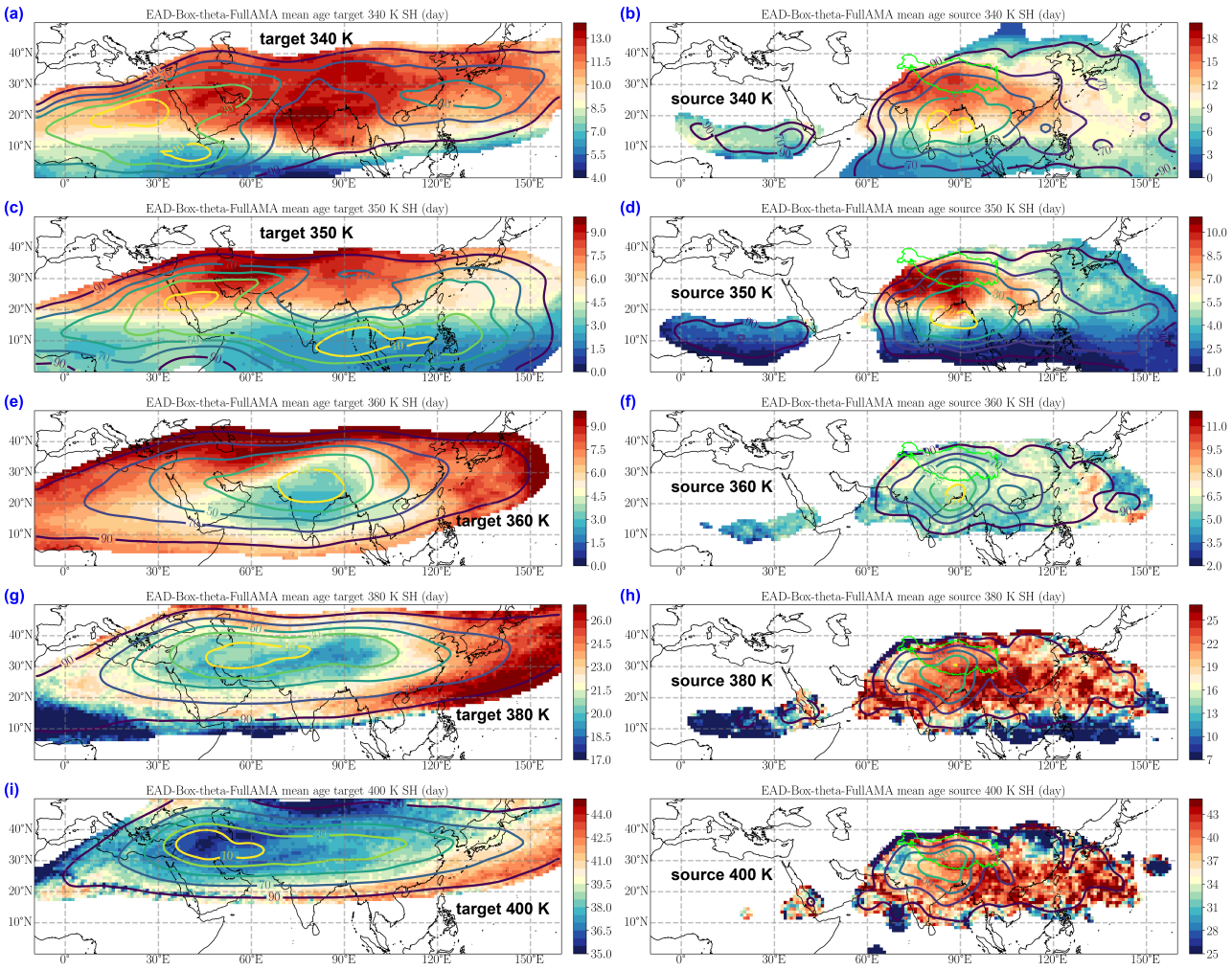

Figure 10. Left column (a,c,e,g,i): mean age (in day) with respect to convection for forward parcels reaching the levels 340 K (a), 350 K (c), 360 K (e), 380 K (g) and 400 K (i). Right column (b,d,f,h,j): mean age in the source domain for the same parcels as in the left column for each level. The contours show the impact distribution at the same level and the fields are clipped outside of the contour that contains 95% of the cumulated impact. The results are shown for the ERA5 forward diabatic trajectories (EAD)

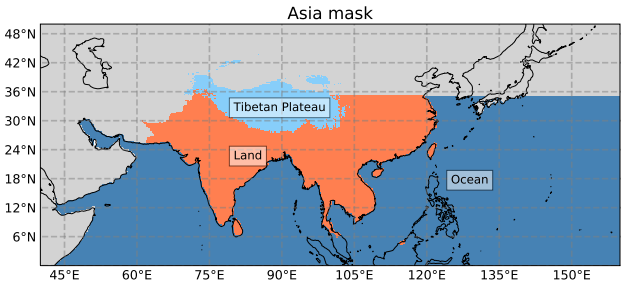

Figure 11. Mask of the three regions that partition Asia defined as their union.

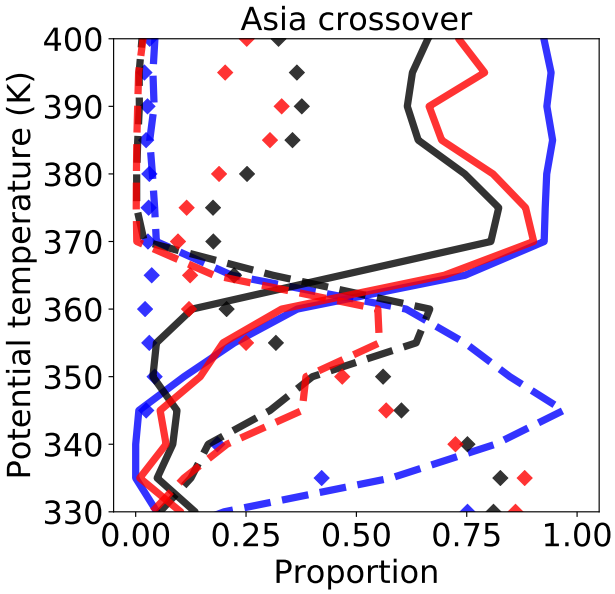

Figure 12. Solid and dashed curves: proportion of forward diabatic trajectories for which the mean vertical position during life-time is in a 5 K bin, respectively above or below, that of origin. Diamonds: proportion of forward trajectories with a mean vertical position within the origin 5 K bin. Black: ERA5 in the FullAMA domain; Red: ERA-Interim in the FullAMA domain. Blue: ERA-Interim in global domain. The curves are plotted for ~~teh~~ the whole Asia domain.

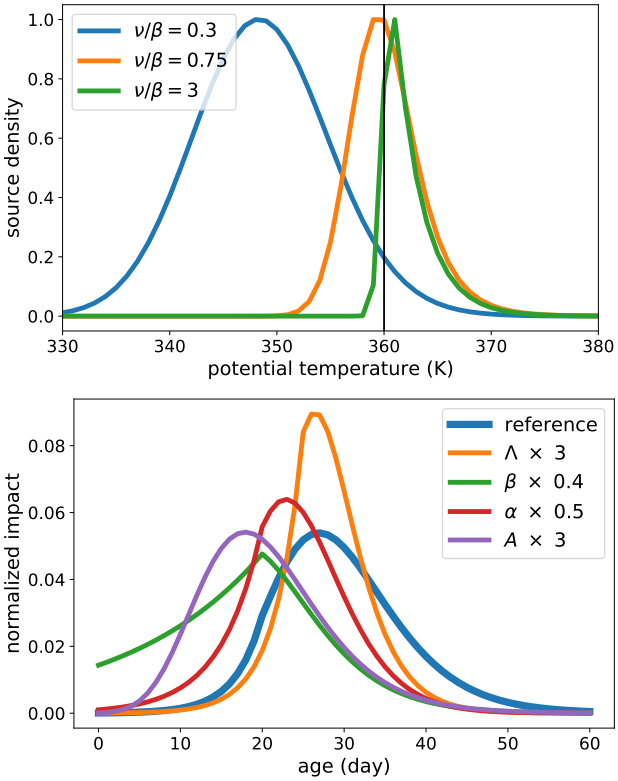

Figure 13. Upper panel: Distribution of convective sources $NP(\theta)$ according to (2) for $\theta_0 = 360$ K, $\beta = 0.4$ K^{-1} and three values of ν/β: 0.3, 0.75 and 3 as indicated in the legend. The proportion of sources above the LZRH θ_0 in the three cases is, respectively, 4.7%, 55.8% and 97.4%. Lower panel: Solution of (1) described by (S5-S7) for the parameters given in the text and modified solutions according to the changes indicated in the legend. Each curve is normalized with respect to its integral in the displayed interval.

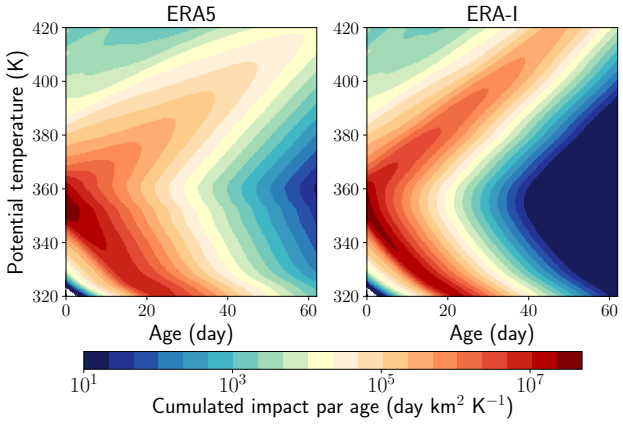

Figure 14. Solution of the equation (1) for the observed distribution of high clouds and heating rates within the ~~CoreAMA~~ restricted region defined in Fig. 4. Left panel for ERA5 is to be compared with the upper right panel of Fig. 5. Right panel for ERA-Interim is to be compared with the lower right panel of Fig. 5.

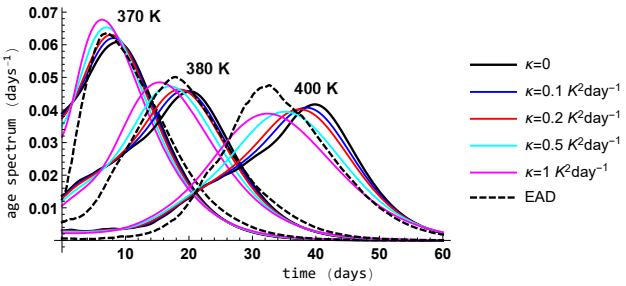

Figure 15. Solution of the equation (1) with the same set-up as in Fig. 14 for the diabatic ERA5 case. The normalized age spectrum is shown from left to right at 370 K, 380 K and 400 K for the inviscid solution (~~D0~~*kappa* = 0) and for four values of the diffusion ~~*K*~~ κ: 0.1 ~~(D01)~~, 0.2 ~~(D01)~~, 0.5 ~~(D05)~~ and 1 ~~(D1)~~$\mathrm{K}^2\mathrm{day}^{-1}$ as indicated in the legend. The normalized age spectrum for the 3D trajectories (EAD) is shown as a reference.

Table 1. Main characteristic numbers for the cloud distribution and the trajectories originating from Asia as a whole and its three sub-regions (Land, Ocean and Tibetan Plateau). When a proportion 100% is in the Asia column, the three other numbers in the row show the contributions of the three regions. EID is not separated into FullAMA and global cases when the distinction does not apply (LZRH and cloud fraction) or when it is negligible (crossover).

		Asia	Land	Ocean	Tibetan Plateau
High clouds SAF	Proportion	100 %	26.6%	68.4%	5.0%
	Max high cloud level	349.5 K	355.5 K	349.5 K	359.5 K
	Mean high cloud level	352.9 K	356.4 K	351.1 K	359.0 K
All sky LZRH	EAD	357.9 K	361.0 K	356.7 K	365.2 K
	EID	352.9 K	357.6 K	351.0 K	366.7 K
Crossover	EAD	363.9 K	364.4 K	362.5 K	364.2 K
	EID	361.7 K	361.8 K	358.5 K	363.1 K
High cloud fraction above crossover	EAD	2.6%	5.1%	1.7%	10.8%
	EID	5.1%	10.4%	4.1%	16.7%
Impact at 380 K and above	EAD FullAMA	100%	54.8%	22.8%	22.4%
	EID FullAMA	100%	54.4%	32.0%	13.6%
	EID global	100%	39.0%	52.9%	8.1%
Mean θ source for impact at 380 K and above	EAD ~~FullAMA~~	366.0 K	366.0 K	367.2 K	364.7 K
	EID FullAMA	362.2 K	362.7 K	360.7 K	364.1 K
	EID global	359.2 K	361.5 K	356.7 K	363.7 K
Proportion of source above LZRH for impact at 380 K and above	EAD ~~FullAMA~~	95.2%	83.5%	95.6%	36.5%
	EID FullAMA	96.5%	87.5%	96.1%	14.2%
	EID global	94.1%	74.1%	81.3%	12.5%